

## The Influence of the Indian Ocean on ENSO Stability and Flavor

CLAUDIA E. WIENERS, HENK A. DIJKSTRA, AND WILL P. M. DE RUIJTER

*Institute for Marine and Atmospheric Research Utrecht, Department of Physics and Astronomy,  
Utrecht University, Utrecht, Netherlands*

(Manuscript received 12 July 2016, in final form 28 November 2016)

### ABSTRACT

The effect of long-term trends and interannual, ENSO-driven variability in the Indian Ocean (IO) on the stability and spatial pattern of ENSO is investigated with an intermediate-complexity two-basin model. The Pacific basin is modeled using a fully coupled (i.e., generating its own background state) Zebiak–Cane model. IO sea surface temperature (SST) is represented by a basinwide warming pattern whose strength is constant or varies at a prescribed lag to ENSO. Both basins are coupled through an atmosphere transferring information between them. For the covarying IO SST, a warm IO during the peak of El Niño (La Niña) dampens (destabilizes) ENSO, and a warm IO during the transition from El Niño to La Niña (La Niña to El Niño) shortens (lengthens) the period. The influence of the IO on the spatial pattern of ENSO is small. For constant IO warming, the ENSO cycle is destabilized because stronger easterlies induce more background upwelling, more thermocline steepening, and a stronger Bjerknes feedback. The SST signal at the east coast weakens or reverses sign with respect to the main ENSO signal [i.e., ENSO resembles central Pacific (CP) El Niños]. This is due to a reduced sensitivity of the SST to thermocline variations in case of a shallow background thermocline, as found near the east coast for a warm IO. With these results, the recent increase in CP El Niño can possibly be explained by the substantial IO (and west Pacific) warming over the last decades.

### 1. Introduction


The El Niño–Southern Oscillation (ENSO) phenomenon in the Pacific Ocean (PO) keeps fascinating the climate research community. Based on the early (sparse) observations, one was led to think in terms of a “canonical” ENSO (Rasmusson and Carpenter 1982; Philander 1990). Nowadays different flavors of initiation, development, and termination have been identified (Capotondi and Sardeshmukh 2015). A major distinction between El Niño events is their zonal extent (Larkin and Harrison 2005; Kug et al. 2009). The central Pacific (CP) type shows high SSTs in the central PO, whereas eastern Pacific (EP) El Niños also have strong warm anomalies in the eastern PO. CP El Niños are thought to have shorter periods (Kao and Yu 2009) and

have become more frequent in recent decades (Ashok et al. 2007).

The formulation of the Zebiak–Cane (ZC) model (Zebiak and Cane 1987) was a breakthrough in understanding ENSO dynamics. In the ZC model, the (steady or seasonal) background climate (e.g., provided by observations) becomes unstable when the strength of the Bjerknes feedback processes, usually represented by  $\mu$ , exceeds a critical value  $\mu_{\text{crit}}$ . This is referred to as a Hopf bifurcation (steady background state) or a Neimark–Sacker bifurcation (seasonal background state). When  $\mu > \mu_{\text{crit}}$ , interannual-time-scale oscillatory motion develops spontaneously (Fedorov and Philander 2000; Bejarano and Jin 2008), and its spatial pattern is usually referred to as the ENSO mode. When  $\mu < \mu_{\text{crit}}$ , the ENSO mode is damped.

The different flavors of temporal ENSO development and spatial patterns may arise as a result of a variation of the strength of the different Bjerknes feedbacks (thermocline, zonal advection, and upwelling), which amplify sea surface temperature (SST) perturbations. Kao and Yu (2009) suggest that CP El Niños are more dominated by local winds and SST advection, whereas in EP events thermocline processes play a greater role. The strength

---

 Denotes content that is immediately available upon publication as open access.

---

Corresponding author e-mail: Claudia E. Wieners, c.e.wieners@uu.nl

DOI: 10.1175/JCLI-D-16-0516.1

© 2017 American Meteorological Society. For information regarding reuse of this content and general copyright information, consult the [AMS Copyright Policy](http://www.ametsoc.org/PUBSReuseLicenses) ([www.ametsoc.org/PUBSReuseLicenses](http://www.ametsoc.org/PUBSReuseLicenses)).

of these feedbacks depends on the background state, which can be influenced by processes outside of the Pacific basin. In [Dijkstra and Neelin \(1995\)](#), these external processes were limited to a zonally averaged wind stress  $\tau_{\text{ext}}^x$ , thought of as the zonal component of the Hadley circulation. It was shown that stability properties of the background state of the ZC model depend strongly on  $\tau_{\text{ext}}^x$ .

Links between El Niño flavors and the Pacific background state have been investigated using global climate models. [Yeh et al. \(2009\)](#) use CMIP3 runs to suggest that increased CO<sub>2</sub> concentrations lead to weakened trade winds, thermocline flattening, and enhanced CP El Niño activity, though [McPhaden et al. \(2011\)](#) found strengthening trades and thermocline steepening in observations for 1980–2010.

ENSO might also be influenced by SST variability in the adjacent tropical Indian Ocean (IO) and Atlantic Ocean (AO). For the AO, [Wright \(1986\)](#) and [Ham et al. \(2013\)](#) suggest that both North and equatorial AO SST initial conditions increase forecasting skill for ENSO. However, [Frauen and Dommenges \(2012\)](#) and [Dommenges et al. \(2006\)](#) suggest that the effect of decoupling the AO on the spectral properties of ENSO (standard deviation and period) is much lower than for decoupling the IO. The reason for this may be that the AO—at least the AO equatorial SST—does not show a consistent response to ENSO ([Chang et al. 2006](#); [Jansen et al. 2009](#)), so the AO influence does not occur at a fixed phase relation to ENSO.

However, the IO shows a strong response to ENSO. The dominant response is a basinwide warming (BWW) of the tropical IO in the boreal spring following El Niño ([Klein et al. 1999](#)). IO SST anomalies feed back on the PO, causing the systematic influence on ENSO amplitude and period found by [Frauen and Dommenges \(2012\)](#). There is evidence that the IO evolves to some extent independently of ENSO ([Saji et al. 1999](#); [Webster et al. 1999](#)), which might lead to the IO increasing the forecasting skill for ENSO (e.g., [Izumo et al. 2010](#)). [Wieners et al. \(2016\)](#) used multichannel singular spectrum analysis of observational data to show that the PO and IO both take part in the ENSO cycle. They show that the observed correlation between the west IO SST and ENSO at 1.5-yr lead time is stronger than one would expect, based purely on the influence of ENSO on the IO (i.e., the IO does not just passively respond to ENSO). They also find evidence that El Niños preceded by a cool west IO 1.5 yr earlier are more likely to be EP El Niños.

The aforementioned studies focus on the effect of interannual variability of the IO on ENSO. However, long-term trends in IO SST may influence the

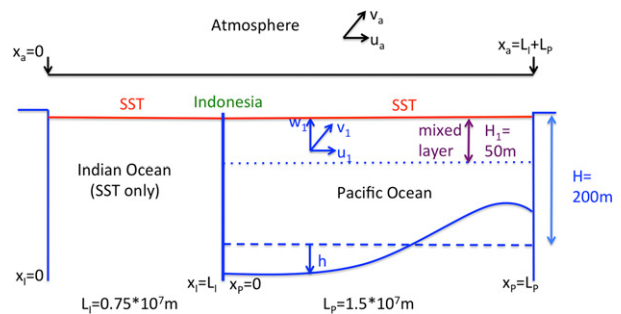


FIG. 1. Cross section along the equator ( $y = 0$ ) of the model configuration with a Zebiak–Cane Pacific Ocean and an idealized Indian Ocean.

background state on the Pacific and therefore the stability and flavor of ENSO ([Luo et al. 2012](#)). The IO has shown a substantial warming over the last few decades. Using HadISST data at 1° resolution ([Rayner et al. 2003](#); [Met Office Hadley Centre 2012](#)), the linear warming trend of the basinwide warming index (BWI; 20°N–20°S, 40°–100°E) for 1970–2011 is  $1.2 \text{ K (100 yr)}^{-1}$ , whereas for 1900–69 this trend is  $0.3 \text{ K (100 yr)}^{-1}$ . For comparison, the corresponding values for Niño-3.4 are  $0.2 \text{ K (100 yr)}^{-1}$  (1970–2011) and  $-0.2 \text{ K (100 yr)}^{-1}$  (1900–69). Though the discrepancies between datasets for the tropical Pacific are large ([Deser et al. 2010](#)), the IO seems to be warming relative to the PO, which may influence the background wind field of the PO and thereby affect ENSO.

In this paper we investigate the influence of large-scale interannual IO variability and long-term IO SST trends on the stability and spatial patterns of ENSO, using a Pacific Zebiak–Cane model extended with a simple Indian Ocean. As our model is fully coupled (i.e., generates its own climatology), changes in the background state can also be studied. We will focus on two questions: 1) Can the recent long-term IO warming explain the more frequent occurrence of CP El Niños? 2) How does ENSO-induced variability in the IO feed back on ENSO? After a brief description of the model (see [section 2](#)), these questions will be addressed in [sections 3b](#) and [3c](#), respectively. A summary and discussion concludes the paper ([section 4](#)).

## 2. Methods

Physically, our model is a convection-free two-basin version of the model by [Zebiak and Cane \(1987\)](#) (ZC model). The oceans are meridionally unbounded and bounded by meridional coast lines; Indonesia is treated as an infinitely thin wall (see [Fig. 1](#)). The IO is half as long as the PO. In [section 2a](#) we describe the PO component of the model. [Section 2b](#) is focused on the

coupling between the IO and PO. The method to analyze the solutions (and their stability) is provided in section 2c.

### a. Pacific model

For the PO component, we use the fully coupled pseudo-spectral version of the ZC model (Van der Vaart et al. 2000). The full (dimensionless) model equations and parameters are given in appendix A. Our model, unlike the one by Zebiak and Cane (1987), generates its own background state. It only requires a weak, external easterly wind stress  $\tau_{\text{ext}}^x$ , which is assumed to be due to the Hadley circulation, independently of SST gradients.

The ocean dynamics in the Pacific is described using a shallow-water reduced-gravity model on the equatorial  $\beta$  plane. It contains an active upper layer with horizontal velocities  $u_r$ ,  $v_r$  and a deep lower layer at rest, separated by a thermocline at depth  $H + h$  where the equilibrium depth  $H = 200$  m. The vertical velocity  $w_r$  is determined by mass conservation. The long-wave limit is applied and damping is assumed to be linear. The shallow-water ocean is forced by the wind stress field  $\boldsymbol{\tau} = (\tau_x, \tau_y)$ . At the eastern boundary, the zonal velocity vanishes, while at the western boundary the mass flux is zero. A mixed layer of depth  $H_1 = 50$  m is embedded into the upper shallow-water layer to incorporate the Ekman velocity  $\mathbf{u}_s$ , also forced by the wind stress  $\boldsymbol{\tau}$  under linear damping. The total horizontal velocity in the mixed layer is given by  $\mathbf{u}_1 = \mathbf{u}_r + \mathbf{u}_s$ .

The (dimensional) Pacific sea surface temperature (SST)  $T_P$  evolves as follows:

$$\begin{aligned} \partial_t T_P + u_1 \partial_{x_p} T_P + v_1 \partial_{y_p} T_P + \frac{w_1}{H} \mathcal{H}(w_1) [T_P - T_{\text{sub}}(h)] \\ + \epsilon_T^* (T_P - T_0) = 0, \end{aligned} \quad (1)$$

where  $\partial_z T_P$  is a shorthand for  $\partial T_P / \partial z$ ,  $x_p$ ,  $y_p$  are the Pacific zonal and meridional coordinates,  $\mathcal{H}$  is the Heaviside function (upwelling only affects the SST if the velocity is upward),  $T_0$  is a prescribed radiative equilibrium temperature, and the subsurface temperature  $T_{\text{sub}}$  is parameterized as

$$T_{\text{sub}}(h) = T_{s0} + (T_0 - T_{s0}) \tanh\left(\frac{h + h_0}{H_*}\right). \quad (2)$$

The SST is influenced by advection [second and third term in (1)], upwelling in the mixed layer (fourth term), and a linearized atmospheric heat flux (fifth term). Parameter values are given in Table 1. A linear, Gill-type atmosphere model (Gill 1980) provides the wind response to SST anomalies. The atmospheric geopotential  $\phi$  is assumed to react instantaneously and linearly to

TABLE 1. Dimensional parameters of the Zebiak–Cane model. (The value of  $\alpha_T \gamma_\tau$  is chosen such that the reference coupling strength  $\mu_0$  in Table A1 lies at the Hopf bifurcation in the reference run.)

Parameter	Meaning
$L_P = 1.5 \times 10^7$ m	PO length
$L_I = 7.5 \times 10^6$ m	IO length
$L_a = L_P + L_I$	Atmosphere length
$H = 200$ m	Background thermocline depth
$H_1 = 50$ m	Mixed layer depth
$c_P = 2$ m s <sup>-1</sup>	Kelvin wave speed (PO)
$c_a = 30$ m s <sup>-1</sup>	Kelvin wave speed (atm)
$\epsilon_\phi^* = 0.42$ yr <sup>-1</sup>	Damping coef ocean dynamics
$\epsilon_\phi^* = 0.22$ day <sup>-1</sup>	Damping coef atm
$\epsilon_s^* = 0.44$ day <sup>-1</sup>	Damping coef Ekman
$\epsilon_T^* = 2.9$ yr <sup>-1</sup>	Damping coef SST
$\tau_0 = 1.1 \times 10^{-2}$ N m <sup>-2</sup>	Background wind strength
$T_0 = 30^\circ\text{C}$	Radiative equilibrium SST
$T_{s0} = 23^\circ\text{C}$	Upwelling temp at $h = h_0$
$h_0 = 30$ m	Offset of $T_{\text{sub}}(h)$
$H_* = 40$ m	Steepness of $T_{\text{sub}}(h)$
$\bar{H} = 50$ m	Mean upwelling depth
$R_P = 3.0 \times 10^5$ m	Rossby radius (PO)
$R_a = 1.5 \times 10^6$ m	Rossby radius (atm)
$\beta = 2.23 \times 10^{-11}$ (m s) <sup>-1</sup>	Beta parameter
$\alpha_T \gamma_\tau = 4.44 \times 10^{-11}$ m <sup>2</sup> (K s <sup>4</sup> ) <sup>-1</sup>	(Wind stress/ $\rho H$ ) per SST anomaly
$\Delta T = 1$ K	Unit SST anomaly

heating induced by departures  $T_I - T_0$  or  $T_P - T_0$  of the SST from the radiative equilibrium, with proportionality constant  $\alpha_T$  and the SST in the IO or PO given by  $T_I$  or  $T_P$ , respectively. Wind stresses depend linearly on the local wind ( $u_a$ ,  $v_a$ ); that is,  $\boldsymbol{\tau} = \gamma_\tau \mathbf{u}_a + \boldsymbol{\tau}_{\text{ext}}$ , where  $\boldsymbol{\tau}_{\text{ext}}$  is the earlier mentioned external contribution (i.e., not affected by SST). Thus, the PO basin can be influenced by the IO basin through the winds induced over the PO by SST anomalies in the IO.

### b. Indian–Pacific Ocean coupling

It is mathematically possible to model the IO with the full ZC model dynamics. However, it is challenging to find a parameter set well suited to describe IO variability in the ZC framework. The IO mean state is not dominated by Bjerknes feedback dynamics (i.e., there is no strong cold tongue in the East), sustaining itself by producing strong easterlies. Reasons for this might include the small length of the IO, the presence of the warm Maritime Continent, and the Asian landmass. In addition, there is a strong seasonal cycle (monsoon) and off-equatorial variability, which is hard to capture within the ZC model.

As our main interest is the influence of the IO on ENSO, we follow an idealized approach wherein the IO SST is completely determined by the state of the PO.

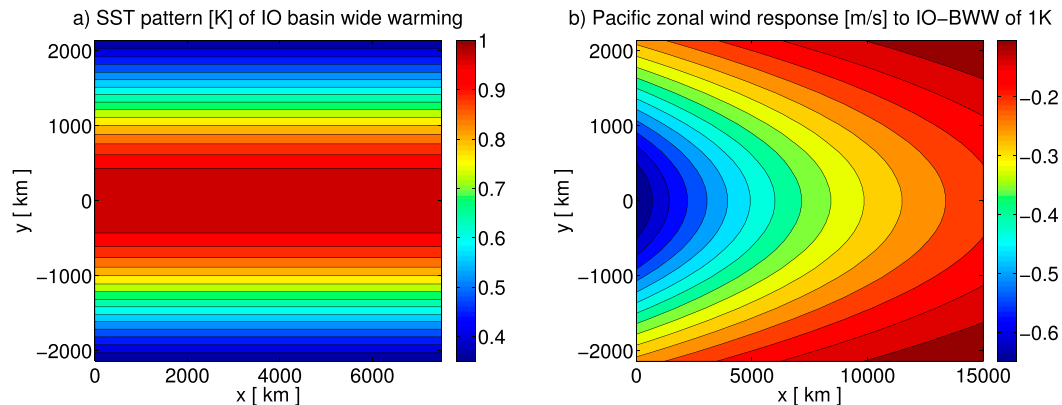


FIG. 2. (a) The Indian Ocean SST pattern  $T_I^0(x_I, y_I)$ . (b) The zonal wind response over the Pacific Ocean associated with  $T_I^0$ ; here coordinates are PO coordinates ( $x = 0$  on the PO west coast).

Therefore, the ocean dynamics of the IO are neglected and the dependence of IO SST on the state of the Pacific is parameterized. This approximation seems justified because of the high correlations between ENSO indices and IO quantities. For example, the correlation between the Indian Ocean BWI (see section 1) in spring and the previous winter's Niño-3.4 index is about 0.75.

The IO SST field  $T_I(x_I, y_I, t)$  is represented as follows:

$$T_I(x_I, y_I, t) = T_0 + T_I^0(x_I, y_I)A(t), \quad (3)$$

where  $T_0$  is the radiative equilibrium temperature,  $T_I^0(x_I, y_I)$  is a fixed spatial pattern of the IO SST anomaly, and  $A(t)$  the time-dependent amplitude of this IO SST anomaly. The term  $T_I^0$  is chosen to be zonally uniform and meridionally Gaussian so as to resemble a BWW of the IO; that is,  $T_I^0(x_I, y_I) = 1 \text{ K} \times \exp[-(\alpha y_I)^2/2]$ . As the atmospheric equations are linear, a positive (warm) BWW pattern will lead to a Gill-type wind response with easterlies over the PO (see Fig. 2).

Apart from BWW, ENSO events are also associated with Indian Ocean dipole (IOD) events. However, this effect is not included into (3) because at least in the linear atmosphere model, the contributions of the two poles of the IOD nearly cancel and the wind response over the PO to an IOD event {e.g., represented by  $T_I^0(x_I, y_I) = 1 \text{ K} \times \arctan[4(x_I - 0.5)] \exp[-(\alpha y_I)^2/2]$ } is only about a factor of 1/7 as strong as the response to the BWW.

The evolution of the BWW amplitude  $A(t)$  is adapted from the conceptual model of Jansen et al. (2009):

$$\frac{dA}{dt} = a_N(N - \bar{N}) + a_{Nt} \frac{dN}{dt} + a_c + a_d A. \quad (4)$$

Here  $N$  is an El Niño index specified in (A9), which describes how well  $T_P - T_0$ , the SST anomaly with

respect to radiative equilibrium in the Pacific, projects onto the El Niño pattern shown in Fig. 3. The term  $a_c$  is a constant forcing term,  $a_d < 0$  a damping parameter, and  $a_N$  and  $a_{Nt}$  determine the influence of  $N$  and its time derivative on  $A$ . The term  $\bar{N}$  is the mean of  $N$  as will be specified later in section 3c. The combination of  $a_N$  and  $a_{Nt}$  makes it possible to control the phase difference between  $A$  and  $N$ .

The parameter choices for the PO component of our model are nearly identical to those in Van der Vaart et al. (2000), and a list of dimensional parameters is given in Table 1. The zonal length of the atmosphere is  $L_a = L_P + L_I = 1.5L_P$ , where  $L_P$  and  $L_I$  are the length of the PO and IO, respectively. Our dimensional SST atmosphere coupling strength  $\alpha_T \gamma_\tau$  is 0.925 times the value of Van der Vaart et al. (2000).<sup>1</sup>

### c. Numerical bifurcation analysis

As in Van der Vaart et al. (2000), the equations are discretized using a pseudo-spectral method. In the PO, the SST difference  $Q_P = T_P - T_0$  and  $r = (u_r + h)/2$  are expanded as follows:

$$Q_P(x_P, y_P, t) = \sum_{i=0}^{n_x} \sum_{j=0}^{n_y} f_{ij}(x_P, y_P) q_{ij},$$

$$r(x_P, y_P, t) = \sum_{i=0}^{n_x} \sum_{j=0}^{n_y} f_{ij}(x_P, y_P) r_{ij}. \quad (5)$$

The base function  $f_{ij}$  is given in appendix A. Only the first  $n_x + 1$  zonal and  $n_y + 1$  meridional modes are

<sup>1</sup> In Van der Vaart et al. (2000) a different scaling is used for the nondimensional coupling strength  $\bar{\mu}$ , so that their values are  $1/6$  of our values. However, the dimensional (hence, physical) quantity  $\alpha_T \gamma_\tau$  differs by a factor of 0.925, as mentioned.

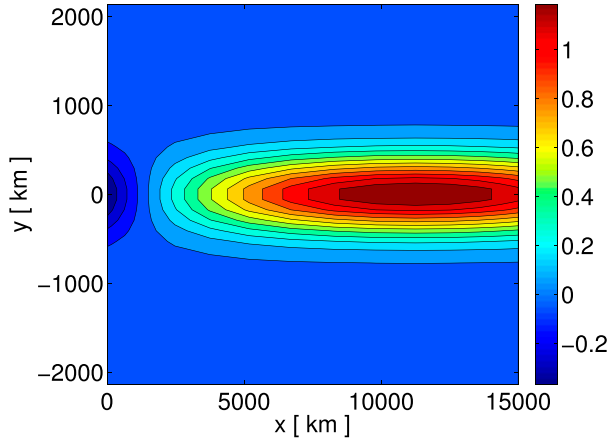


FIG. 3. Spatial SST pattern in the Pacific Ocean associated with the El Niño index  $N$ . High positive values of  $N$  mean that the SST anomaly field projects strongly onto this pattern (El Niño). The coordinate  $x = 0$  is located at the west coast of the PO and  $y = 0$  indicates the equator.

included. The spectral coefficients  $q_{ij}$  and  $r_{ij}$  in the PO and the SST amplitude  $A(t)$  in the IO suffice to describe the whole model system and form the  $d \equiv 2(n_x + 1)(n_y + 1) + 1$ -dimensional state vector  $z$ . We investigate how equilibrium (steady) solutions and their linear stability change with certain model parameters. We write the equations for  $z$  (as in appendix A) in the general form:

$$\frac{dz}{dt} = G(z, p). \quad (6)$$

To determine branches of steady solutions of these equations as one of the parameters, denoted by  $p$ , is varied, the pseudo-arclength method of Keller (1977) is used.

Introducing a small perturbation around an equilibrium state  $\bar{z}$  (i.e.,  $z = \bar{z} + \tilde{z}$ ), the linearized version of (6) becomes

$$\frac{d\tilde{z}}{dt} = J\tilde{z}, \quad (7)$$

where  $J$  is the Jacobian of  $G$  (i.e.,  $J_{kl} = \partial G_k / \partial z_l$ ). The solution of (7) is  $\tilde{z}(t) = \exp(Jt)\tilde{z}(0)$ , and hence the equilibrium is stable (all initial perturbations decay) if all eigenvalues  $\sigma = \sigma_r + i\sigma_i$  of  $J$  have negative real parts. At a Hopf bifurcation, a complex conjugate pair of eigenvalues of  $J$  crosses the imaginary axis.

### 3. Results

In this section,  $x$  and  $y$  denote PO basin coordinates with  $x = 0$  at the west coast,  $x = L_P = 1.5 \times 10^4$  km at the east coast, and  $y = 0$  at the equator.

#### a. Reference case

In the reference case, the effect of the IO is switched off (i.e.,  $A = 0$ ), and hence  $T_I = T_0$ . The results are then the same as for the original, PO-only ZC model (Van der Vaart et al. 2000). For the parameters as in Table 1, the Hopf bifurcation of the ENSO mode occurs at  $\tilde{\mu} = \mu_0$  (i.e., at  $\mu \equiv \tilde{\mu}/\mu_0 = \mu_{\text{crit}} = 1$ ; Fig. 4a, for  $A = 0$ ). The period  $P$  of the ENSO mode at  $\mu_{\text{crit}}$  is 4.0 yr (Fig. 4b).

The SST, thermocline depth, and upwelling equilibrium fields at  $\mu_{\text{crit}}$  are shown in Figs. 5d–f. The equilibrium state has a cold tongue with the lowest temperature  $\bar{T}_m = 25^\circ\text{C}$  at  $x = \bar{x}_m = 1.36 \times 10^4$  km,  $y = 0$ . The thermocline becomes as shallow as 167 m (33 m above the reference value  $H = 200$  m) at the east coast, and the strongest equatorial upwelling of  $100 \text{ cm day}^{-1}$  occurs at  $x \approx 1.18 \times 10^4$  m.

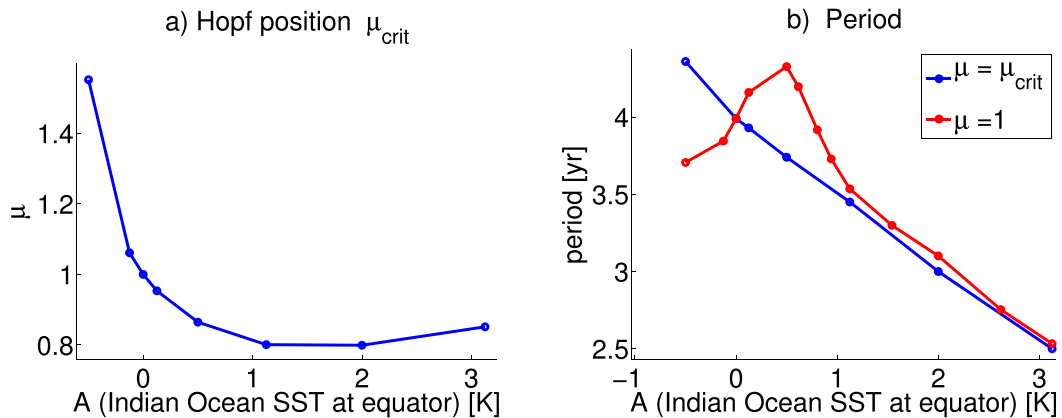


FIG. 4. (a) The position of the Hopf bifurcation  $\mu_{\text{crit}}$  and (b) ENSO period at  $\mu = 1$  (red) and  $\mu = \mu_{\text{crit}}$  (blue) for constant Indian Ocean SST;  $A(t) = +1$  amounts to an IO SST of 1 K above radiative equilibrium at the equator.

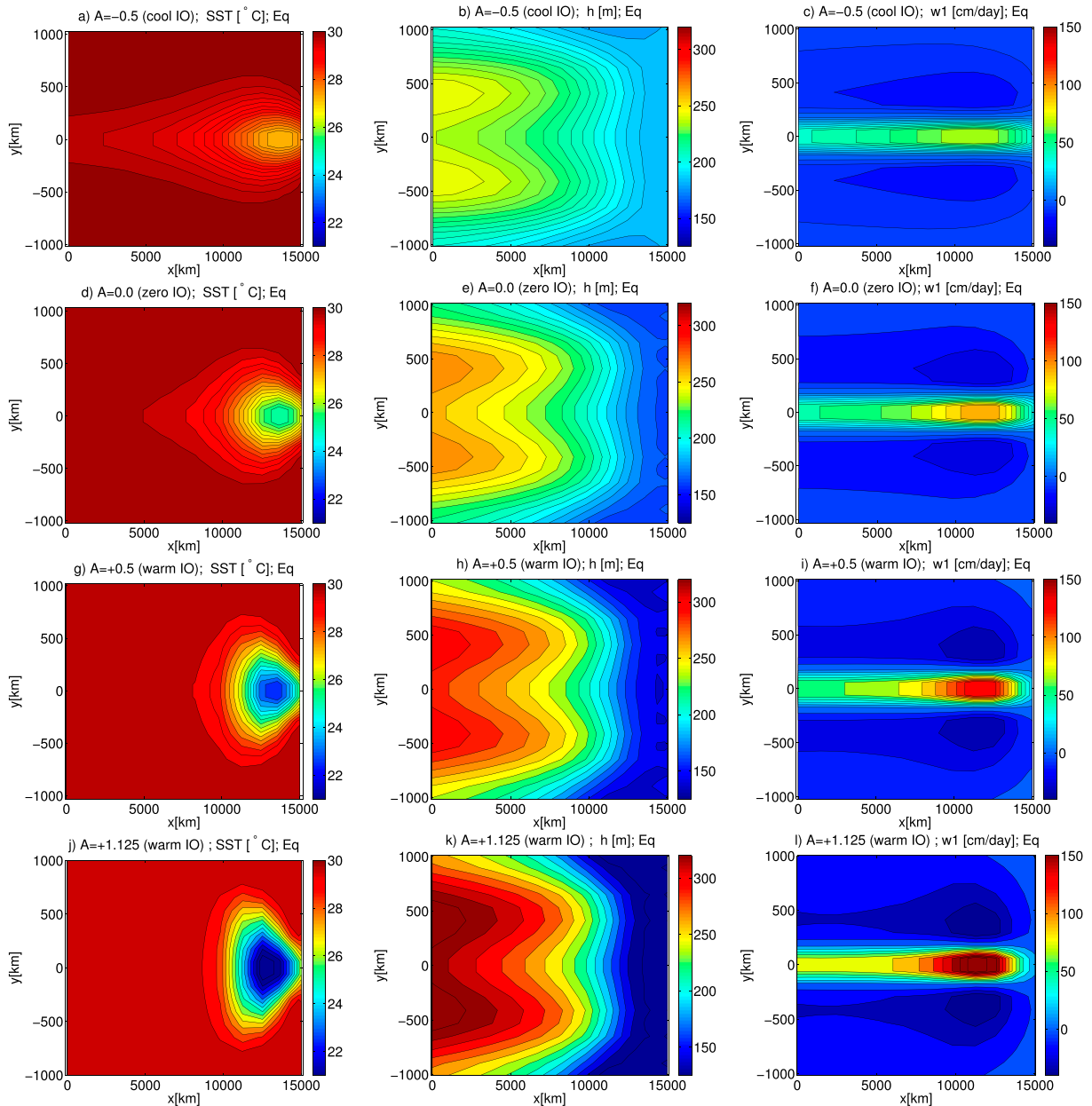


FIG. 5. Equilibrium solutions for the constant IO cases at  $\mu = 1$ . (a) SST (in  $^{\circ}\text{C}$ ), (b) thermocline depth (in m below sea level), and (c) upwelling (in  $\text{cm}/\text{day}$ ) for  $A = -0.5$ . As in (a)–(c), but for (d)–(f)  $A = 0$ , (g)–(i)  $A = +0.5$ , and (j)–(k)  $A = +1.125$ .

The SST field of the eigenvectors at this Hopf bifurcation are plotted in Figs. 6c,d. To characterize the zonal shape of SST anomalies, we define a measure

$$\tilde{\gamma}_{\text{EM}} \equiv \tilde{T}_E / \tilde{T}_M, \quad (8)$$

where  $\tilde{T}_E$  is the equatorial amplitude of the SST anomaly at the east coast, while  $\tilde{T}_M$  is the largest equatorial SST amplitude found (typically at the position  $\tilde{x}_M \approx 1.3 \times 10^4$  km,  $\tilde{y}_M = 0$ ). So  $\tilde{\gamma}_{\text{EM}}$  measures the

strength of the ENSO signal near the coast; the lower the value of  $\tilde{\gamma}_{\text{EM}}$ , the weaker the coastal signal. In addition, we define the phase difference between the coastal and  $x = \tilde{x}_M$  signal as follows:

$$\Delta\phi_{\text{EM}} = \phi_E - \phi_M, \quad (9)$$

which is positive if the signal at the east coast is leading. The reference case has  $\tilde{\gamma}_{\text{EM}} = 0.36$ , (i.e., the ENSO amplitude at the coast is only about  $1/3$  of

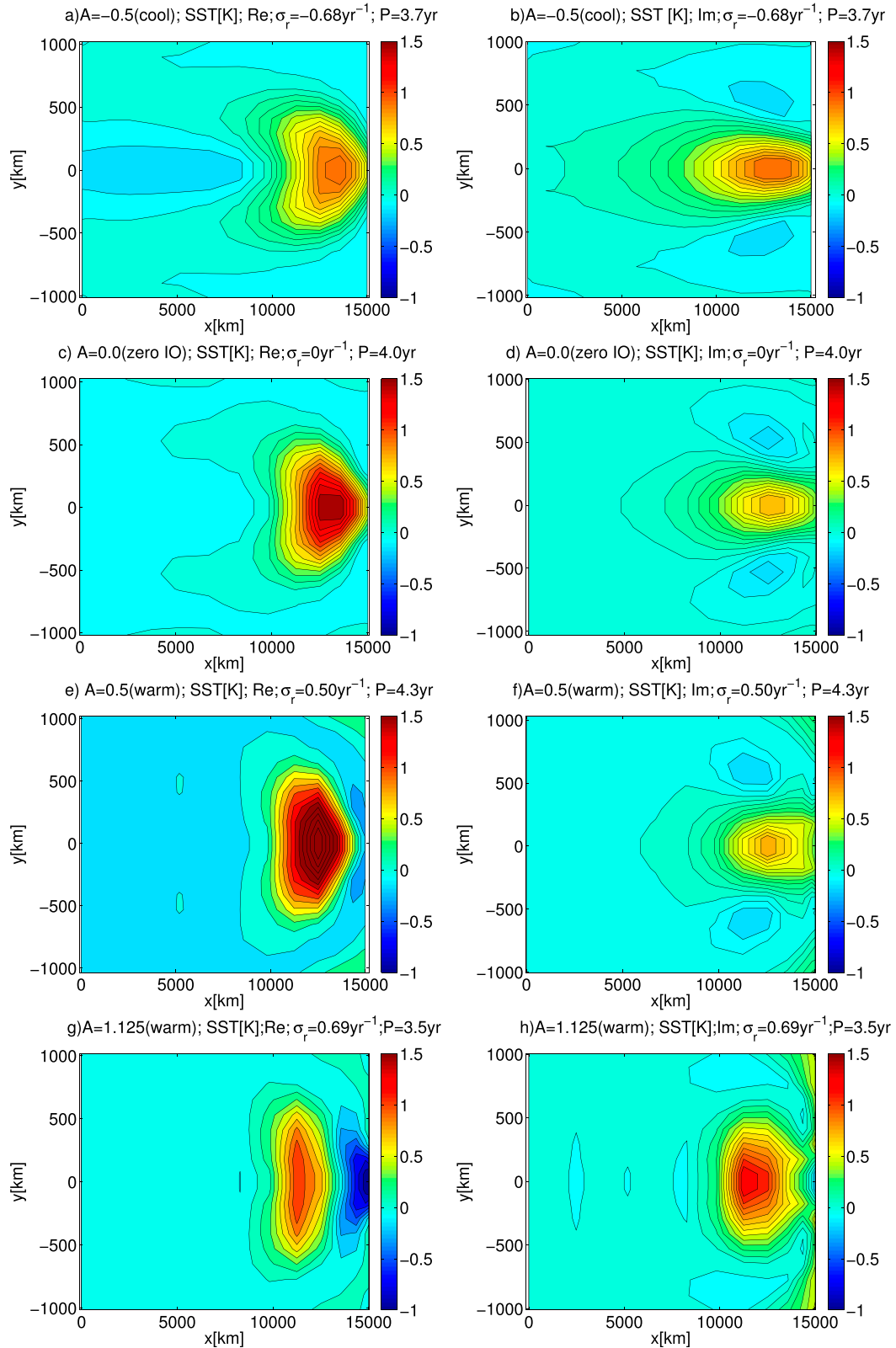


FIG. 6. The SST pattern of the ENSO eigenvectors for constant IO runs at  $\mu = 1$ . (a) Real part and (b) imaginary part for  $A = -0.5$ ; as in (a),(b), but for (c),(d)  $A = 0.0$ , (e),(f)  $A = +0.5$ , and (g),(h)  $A = +1.125$ . The growth rate  $\sigma_r$  is the real part of the eigenvalue, and the period  $P$  is given by  $2\pi/\sigma_i$ , where  $\sigma_i$  is the imaginary part of the eigenvalue. In all plots,  $\sigma_i > 0$ , so the imaginary part of the eigenvector leads the real part.

the amplitude at  $\tilde{x}_M = 1.29 \times 10^4$  km). The phase difference is  $\Delta\phi_{EM} = 10^\circ = 0.03P$  (i.e., the coastal and offshore signal are nearly in phase).

A measure similar to  $\tilde{\gamma}_{EM}$  can be defined to characterize the shape of the background cold tongue:

$$\bar{\gamma}_{Em} \equiv (\bar{T}_E - T_0)/(\bar{T}_m - T_0), \quad (10)$$

where  $\bar{T}_E$  is the equilibrium SST at  $(x = L_P, y = 0)$ , and  $\bar{T}_m$  the lowest temperature found in the cold tongue of the background state, at  $x = \bar{x}_m$ . For the equilibrium state,  $\bar{\gamma}_{Em} = 0.7$  and  $\bar{x}_m = 1.35 \times 10^4$  km. The El Niño index  $N$  of the equilibrium state takes the value  $\bar{N}_{ref} = -4.19$ .

### b. Constant Indian Ocean SST

To investigate the effect of the IO on ENSO, continuation computations are performed to determine Hopf bifurcations at other values of the parameters, starting from the reference case at the Hopf bifurcation, as discussed in the previous section. In the following, the full nondimensional coupling strength  $\tilde{\mu}$  (see Table A1 in appendix A) will be given in terms of the coupling strength  $\mu_0$  at which the Hopf bifurcation occurs in the reference case (i.e.,  $\tilde{\mu} = \mu_0\mu$ ).

We first consider the case  $a_N = A_{Nt} = 0$  in (4) such that  $T_I$  is nonzero but constant. This yields  $T_I(y=0) - T_0 = A = -a_c/a_d$ . As shown in Fig. 4a, the Hopf bifurcation shifts to higher (lower) values of  $\mu$  for a cool (warm) IO. For  $A \lesssim -0.5K$ , the Hopf bifurcation value shifts to large values of  $\mu$  indicating a strong stabilization. At  $A \approx 2$ ,  $\mu_{crit}$  reaches a minimum of 0.80 and then slowly increases again. The period at  $\mu = 1$  (red curve in Fig. 4b) has a maximum of 4.3 yr for  $A \approx 0.5$ . For  $\mu = \mu_{crit}$  the period is lower (higher) than at  $\mu = 1$  for warm (cool) IO (blue curve in Fig. 4b). As a constant warm IO adds a constant easterly wind stress, which is similar to increasing  $\tau_{ext}$ , the results are in qualitative agreement with those in Van der Vaart et al. (2000). They found that  $\mu_{crit}$  first decreases, then saturates with  $\tau_{ext}$  and that both for very low and very high  $\tau_{ext}$  the period decreases (Van der Vaart et al. 2000, their Fig. 14) at fixed  $\mu$ . They also found that the period increases with  $\mu$ .

The value of  $T_I$  affects not only the stability but also the spatial patterns of the associated SST anomalies. Figure 6 shows the SST patterns of the ENSO mode [the eigenvector of the Jacobian in (7) with the largest real part], for  $A \in \{-0.5, 0.0, 0.5, 1.125\}$ . To exclude the influence of  $\mu$  itself, all plots are for  $\mu = 1$ . So for  $A = -0.5$  the ENSO mode is damped (the real part of the eigenvalue  $\sigma_r$  is negative; see Table 2), whereas for  $A > 0$  the ENSO mode grows. For a cool IO, SST anomalies are zonally more elongated, while for a warm IO, they are more compact and detached from the east coast.

TABLE 2. The measures characterizing the ENSO mode and the mean state characterizing the cold ( $A = -0.5$ ), zero ( $A = 0$ ), and warm ( $A = 0.5, A = 1.125$ ) IO cases, all at  $\mu = 1$ . The first four measures describe the ENSO mode:  $\sigma_r$  is the growth factor,  $\tilde{x}_M$  the zonal coordinate of the maximal SST amplitude,  $\tilde{\gamma}_{EM}$  the ratio between the SST amplitude at the east coast and at  $\tilde{x}_M$ , and  $\Delta\phi_{EM}$  the lag between the SST at the east coast and at  $\tilde{x}_M$  (positive if the coastal signal is leading), measured in ENSO periods  $P$ . The next four measures characterize the background state:  $\bar{T}_m$  is the lowest SST in the cold tongue,  $\bar{x}_m$  the zonal location of  $\bar{T}_m$ ,  $\bar{\gamma}_{Em}$  the ratio between the mean SST at the coast and  $\bar{T}_m$ , and  $\bar{\gamma}_{Em,upw}$  is defined as  $\bar{\gamma}_{Em}$  but for the mean upwelling  $\bar{w}_1$  rather than SST. Finally,  $(\lambda_{zadv})/(\lambda_{the} + \lambda_{upw})$  is the ratio between the contributions of zonal advection and thermocline plus upwelling processes to the Bjerknes feedback. Units are shown in brackets.

	$A$	-0.5	0.0	+0.5	+1.125
$\sigma_r$ [yr <sup>-1</sup> ]		-0.67	0.0	+0.5	+0.69
$\tilde{x}_M$ [10 <sup>4</sup> km]		1.32	1.29	1.26	1.17
$\tilde{\gamma}_{EM}$		0.56	0.36	0.15	0.61
$\Delta\phi_{EM}$ [P]		0.02	0.03	0.27	0.39
$\bar{T}_m$ [°C]		27.7	25.1	22.4	20.1
$\bar{x}_m$ [10 <sup>4</sup> km]		1.37	1.36	1.33	1.28
$\bar{\gamma}_{Em}$		0.80	0.70	0.56	0.38
$\bar{\gamma}_{Em,upw}$		0.53	0.36	0.19	0.085
$(\lambda_{zadv})/(\lambda_{the} + \lambda_{upw})$		0.16	0.27	0.54	0.84

To quantify this, the results for the position of maximal SST amplitude  $x_M$ , the ratio between coastal and maximal ENSO amplitude  $\tilde{\gamma}_{EM}$  [see (8)] and the phase difference  $\Delta\phi_{EM}$  (9) are given in Table 2. With increasing  $A$ ,  $x_M$  shifts westward and the SST anomaly directly at the coast is nearly in phase with the signal at  $x_M$  for cool and neutral IO but weakens when  $A$  is increased. For a very warm IO, the coastal signal becomes stronger again, but the phase difference approaches 0.5 (i.e., the SST at the coast has a minimum shortly after the SST at  $x_M$  reaches its maximum). So while for low IO temperatures the ENSO mode resembles the EP El Niño pattern, increasing the IO temperature leads to a more CP-like ENSO mode.

In the  $y$  direction, SST anomalies broaden with increasing  $A$ . The amplitude of thermocline depth anomalies (Fig. 7c) becomes narrower from  $A = +0.5$  to  $A = +1.125$ . For lower  $A$  such a statement is hard to make since at least for  $A = -0.5$  a midlatitude basin mode (Cessi and Paparella 2001) with strong off-equatorial  $h$  variability is mixed into the ENSO mode. The narrowing  $h$  anomalies between  $A = 0.5$  and 1.125 explains the decreasing period (Fig. 4b), as broader  $h$  signals indicate a stronger contribution from higher, and hence slower, Rossby modes (Kirtman 1997).

$T_I$  also affects the mean state (Fig. 5; Table 2). The cold tongue in the eastern PO is much weaker for the cool IO than for the warm IO. The zonal position  $\bar{x}_m$  of the SST minima slightly shifts westward with increasing



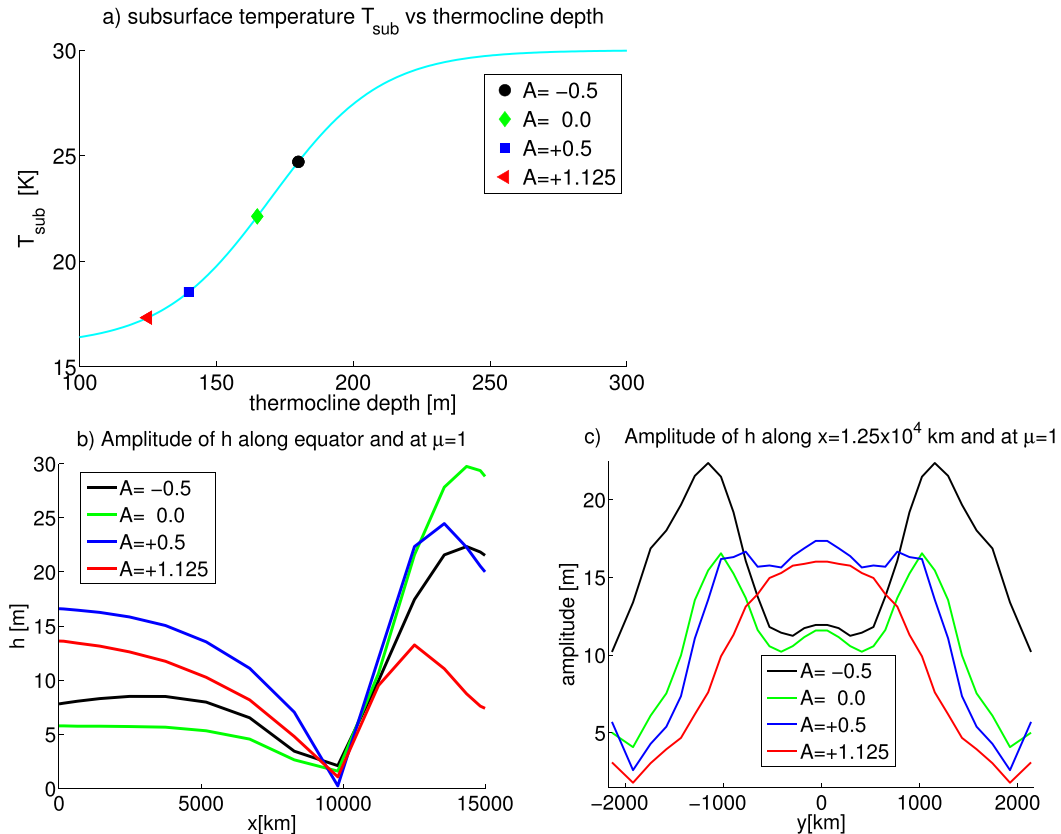


FIG. 7. (a) Dependence of the subsurface temperature  $T_{\text{sub}}$  on thermocline depth  $h$ . The markers denote the conditions found at the east coast on the equator for the  $A = -0.5$  (black circle),  $A = 0$  (green diamond),  $A = 0.5$  (blue square), and  $A = 1.125$  (red triangle); (b) amplitudes of  $h$  along the equator (obtained from the ENSO eigenvector) for  $A = -0.5$  (black),  $A = 0$  (green),  $A = 0.5$  (blue), and  $A = 1.125$  (red). (c) As in (b), but along  $x = 1.25 \times 10^4$  km.

$A$ , and like the SST anomalies, the equilibrium cold tongue becomes more zonally confined with increasing  $A$ , as reflected by the decrease in  $\bar{\gamma}_{\text{Em}}$  [see (10)]. In addition, the cold tongue becomes wider in the meridional direction. The equilibrium solution of the thermocline has a similar spatial pattern for all cases, but the thermocline slope is far greater for warm IO. Likewise, the equilibrium upwelling is strongest for the warm IO. The strongest upwelling is found at  $x = 1.13 \times 10^4$  km in all cases, but again the ratio between coastal and maximal value  $\bar{\gamma}_{\text{Em,upw}}$  strongly decreases with increasing  $A$ .

These results can be understood using the fact that a warm IO enhances the mean easterlies over the PO, causing a stronger background equatorial upwelling  $\bar{w}_1$  and a steeper thermocline (Fig. 5). In case of stronger  $\bar{w}_1$ , thermocline anomalies have a stronger effect on the SST, enhancing the thermocline feedback, and vice versa. This explains the shift of the Hopf bifurcation to lower  $\mu$  in the warm IO case, as a weaker SST–atmosphere coupling suffices to generate self-sustained

oscillations if other components of the Bjerknes feedback are strengthened. In addition, a steeper thermocline and stronger  $\bar{w}_1$  strengthen the cold tongue (Fig. 5). For a very cool IO with  $T_{\text{IO}} \lesssim -0.5$  K the background state cold tongue in the east PO cannot maintain itself but shifts to the west PO. Increasing easterlies also strengthen poleward surface currents, and hence meridional advection, which explains the meridional broadening of both the anomalous and the equilibrium SST signal with increasing  $A$ .

These arguments are confirmed with the analysis of the Bjerknes feedback terms (Fig. 8; for computational details, see appendix B). The thermocline term, which is due to anomalies in  $T_p - T_{\text{sub}}(h)$ , is dominant and increases with  $A$ . The upwelling feedback due to anomalies in  $w_1$  also increases from  $A = -0.5$  to  $A = 0$ . The ratio of zonal advection to the sum of thermocline and upwelling terms,  $(\lambda_{\text{zadv}})/(\lambda_{\text{thc}} + \lambda_{\text{upw}})$ , strongly increases with  $A$  (Table 2) until for  $A = 1.125$  advection contributes almost as strongly to the growth factor as

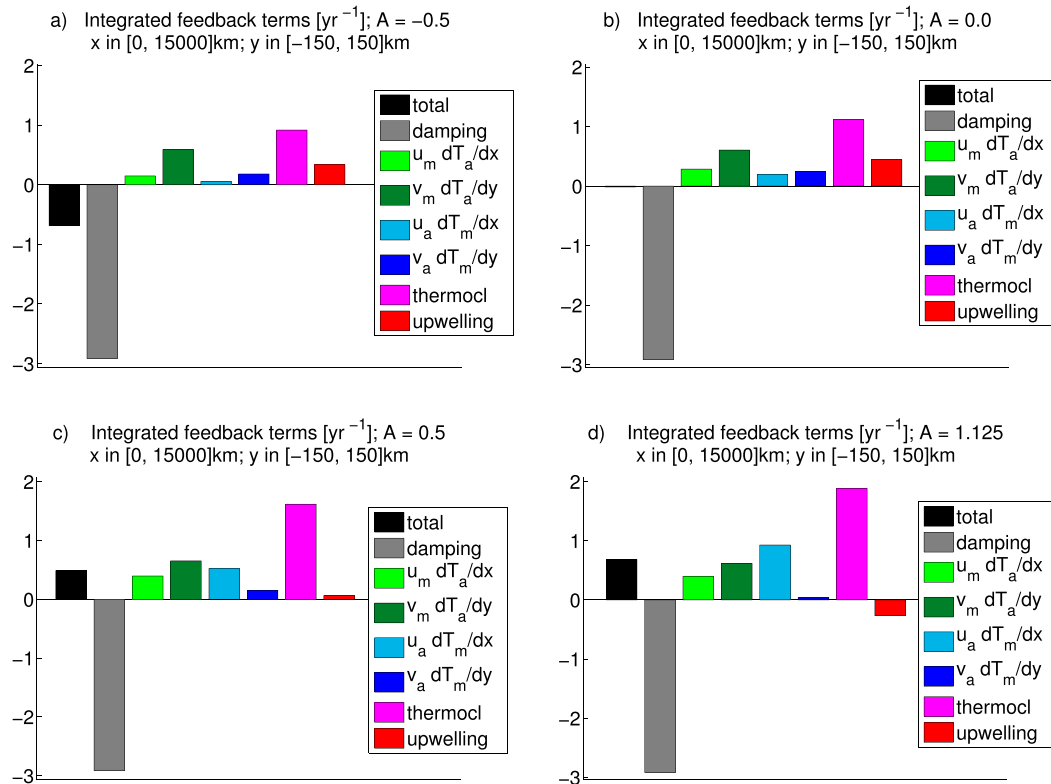


FIG. 8. Bjerknes feedback contributions for (a)  $A = -0.5$ , (b)  $A = 0$ , (c)  $A = 0.5$ , and (d)  $A = 1.125$ , all at  $\mu = 1$ . In all plots, the bars indicate (from left to right) the total growth factor (black), damping (gray), and zonal and meridional advection of SST anomalies by equilibrium currents (light and dark green), zonal and meridional advection of equilibrium SST by anomalous currents (light and dark blue),  $T_p - T_{\text{sub}}$  anomalies (thermocline feedback; magenta), and upwelling anomalies (red).

thermocline and upwelling processes. The fact that advection does not actually become stronger than vertical processes may be due to the fact that the ZC model is quite thermocline-feedback dominated. Partially, this increase in zonal advection terms is explained by stronger equilibrium currents and a more intense cold tongue. In addition, since for high  $A$  the SST anomalies become more zonally confined, the zonal SST gradients increase relative to the magnitude of the SST signal [larger  $(\partial_x T)/T$ ]. Zonal winds and currents increase accordingly. Both the increase in SST gradients and zonal currents (anomalous or equilibrium) leads to increased zonal advection. Meridional advection, which mainly leads to a poleward extension of SST signals generated at the equator, is hardly affected by  $A$ . The stronger meridional equilibrium currents are partially compensated by decreased meridional SST gradients due to broader signals.

To understand the increase in  $\mu_{\text{crit}}$  for very large  $A$  (Fig. 4a) and the changes in spatial patterns, we consider the parameterization of  $T_{\text{sub}}$ , the temperature of upwelled water. According to (2),  $T_{\text{sub}}(h)$  becomes saturated

for very high or low  $h$ . For a shallow thermocline, as found in the eastern PO in the warm IO cases,  $dT_{\text{sub}}/dh$  is considerably smaller than in the cool IO case (Fig. 7a), which reduces the influence of  $h$  anomalies on the SST. This reduction in the thermocline feedback explains why  $\mu_{\text{crit}}$  does not decrease further when  $A$  is increased beyond  $\approx 2$ .

For cool and zero IO, thermocline anomalies have a relatively strong effect near the east coast as their amplitude peaks near the coast (Fig. 7b). Here,  $dT_{\text{sub}}/dh$  is large and the background upwelling  $\bar{w}_1$  at the coast is not much weaker than offshore. For warmer IO, the amplitude of the  $h$  anomaly and  $dT_{\text{sub}}/dh$  near the coast decrease and the difference in  $\bar{w}_1$  between the coast and  $x = 1.13 \times 10^4$  km increases, so the coastal SST amplitudes weaken relative to the offshore ones (lower  $\tilde{\gamma}_{\text{EM}}$ ). If the thermocline is quite shallow and  $T_{\text{sub}}$  is near saturation in the whole eastern PO (say, east of  $x = 1.2 \times 10^4$  km), the location of the strongest SST amplitude ( $x_M$ ) is dominated by the amplitude of the upwelling  $w_1$ . Equatorial upwelling tends to be stronger (weaker) to the west (east) of cool SSTs because of the

SST-induced easterlies (westerlies). This further increases the westward shift of  $x_M$  and the reduction in  $\tilde{\gamma}_{EM}$ , as the warm (cool) offshore SST anomalies during El Niño (La Niña) cause upwelling (downwelling) and hence cooling (warming) near the coast.

For  $A = 1.125$  this effect is so strong that the coastal signal is nearly in antiphase with the offshore variability. This is in line with [Kao and Yu \(2009\)](#), who find that CP El Niños are more dominated by local wind, while EP El Niños are more related to thermocline processes. It also explains the negative contribution of upwelling feedback to the growth factor for  $A = 1.125$  ([Fig. 8d](#)). The upwelling anomalies have their strongest effect on SST near the east coast (strong zonal SST gradients and hence strong winds) and are nearly in antiphase with the main, offshore El Niño signal. Locally, the upwelling term does enhance the (coastal) SST signal.

Similar arguments can be used to explain how  $T_{sub}$  saturation and the effect of low (equilibrium) SSTs in the cold tongue on the wind and hence the upwelling lead to a more offshore cold tongue for warm IO.

We confirmed that the IO-induced decrease in  $\mu_{crit}$  leads to a significant increase in ENSO variability by performing time integrations at  $\mu = 0.86$  (below the Hopf bifurcation for  $A = 0$ ) and with a simple wind noise (spatially Gaussian, centered around  $x_P = L_P/2$ ,  $y_P = 0$ , temporally white noise at a time step of 2.5 weeks, and a standard deviation of  $1.5F_0$ ). The resulting standard deviation of  $N$  was found to be 0.79 for  $A = -0.5$ , 1.57 for  $A = 0$ , and 2.93 for  $A = +1$ .

### c. Covarying Indian Ocean SST

Next, the case is considered wherein  $T_I$  covaries with the Pacific ENSO cycle. The most realistic phase relation between ENSO and IO SST is that  $T_I$  peaks a few months after  $N$ . However, in order to better understand the behavior of the coupled IO–PO system, four cases are considered, wherein  $T_I$  peaks shortly after the maximum of  $N$  [i.e., during the decay of El Niño (ED)], shortly after the minimum of  $dN/dt$  [i.e., during the growth of La Niña (LG)], after the minimum of  $N$  [i.e., during the decay of La Niña (LD)], or after the maximum of  $dN/dt$  [i.e., during El Niño growth (EG)].

For the ED and LD cases, (4) takes the form

$$\frac{dA}{dt} = \pm a_0(N - \bar{N}) + a_d A, \quad (11)$$

where the upper (lower) sign corresponds to the ED (LD) case, and  $a_0 > 0$  scales the effect of the IO. If one performs a continuation in  $a_0$  from  $a_0 = 0$  and chooses  $\bar{N}$  to equal  $N(a_0 = 0)$ , then  $A = 0$  remains the equilibrium solution for  $A$  (in physical terms,  $A$  is zero mean), so the IO does not affect the equilibrium state. But the

eigenvectors and eigenvalues—hence the stability of the equilibrium—are affected. As we start our continuation from the Hopf bifurcation of the reference case,  $\bar{N} = \bar{N}_{ref} = -4.19$  is chosen.

For the EG and LG cases, (4) becomes

$$\frac{dA}{dt} = \pm \frac{a_0}{\omega} \frac{dN}{dt} + a_d A, \quad (12)$$

where the upper (lower) sign corresponds to the EG (LG) run and  $\omega$  is the angular frequency of the ENSO mode. The choice of  $a_{Nr} = a_0/\omega$  ensures that the effect of ENSO on  $A$  has the same scale in (11) and (12), since in a harmonic oscillation  $N$  and  $1/\omega dN/dt$  have the same amplitude. As  $\omega$  is not known a priori, the value of the reference case is chosen; that is,  $\omega = \omega_{ref} \equiv 2\pi/(4.0 \text{ yr})$ . Again,  $A = 0$  in the equilibrium solution and the IO only affects the stability of the equilibrium state.

For all covarying IO cases,  $a_d = 3.8 \text{ yr}^{-1}$  is chosen. It can be shown that with  $\omega = \omega_{ref}$  this leads to a phase difference  $\psi$  between  $N$  and  $A$  of  $\psi = \arctan(-\omega/a_d) = 22^\circ + n \times 90^\circ$ , where  $n = 0, 1, 2, 3$  in the ED, LG, LD, and EG cases, respectively. For example, in the EG case, as long as the period remains close to the 4 yr of the reference run, the IO SST peaks about 3 months (1/16 cycle) after  $N$ . Also, for  $a_0 = 0.98 \text{ yr}^{-1}$  the amplitude of  $T_{IO}(x, y = 0, t)$  is about  $1/4$  of the amplitude of  $N$ .

As can be seen from [Fig. 9a](#), the ENSO mode is stabilized for the ED and EG cases and destabilized for the LD and LG cases. At  $a_0 = 0.98 \text{ yr}^{-1}$ ,  $\mu_{crit}$  increases to 1.27 and 1.21 for the ED and EG cases, respectively, while for the LD and LG cases,  $\mu_{crit}$  is reduced to 0.85 and 0.60, respectively. By construction, the period at  $\mu = \mu_{crit}$  ([Fig. 9b](#)) of the ENSO mode is 4.0 yr for  $a_0 = 0$ . For ED and LG, the period at the Hopf bifurcation is reduced to 2.9 and 2.24 yr, respectively, while in the LD and EG cases the period increases to 7.1 and 7.4 yr, respectively.

Performing a continuation in  $\mu$  away from  $\mu = 1$  can cause  $\bar{N}$ , the true equilibrium value of  $N$ , to deviate from  $\bar{N}_{ref}$ , the estimate for  $\bar{N}$  used in (11). In the ED and LD cases, this leads to a nonzero equilibrium solution of  $A$ , with a value of  $\mp a_0(\bar{N} - \bar{N}_{ref})/a_d$ . To estimate whether the shifts in  $\mu_{crit}$  ([Fig. 9a](#)) and period at  $\mu = \mu_{crit}$  ([Fig. 9b](#)) in the ED and LD cases are due to the constant or to the oscillatory contribution to  $A$ , a control case was performed with

$$\frac{dA}{dt} = \pm a_0(\bar{N} - \bar{N}_{ref}) + a_d A \quad (13)$$

(i.e., with a constant  $A$  equal to the error arising from the shift in  $\bar{N}$ ). The results of these control cases for  $a_0 = 0.98 \text{ yr}^{-1}$  are shown as unfilled markers in [Figs. 9a,b](#).

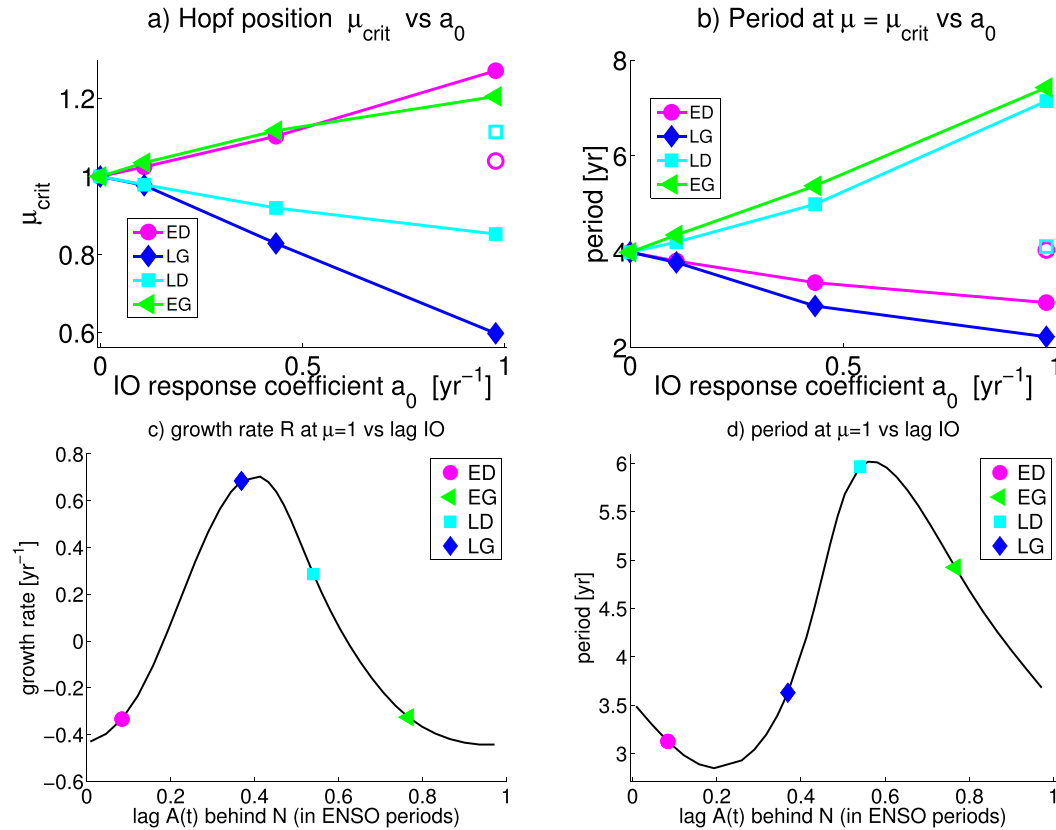


FIG. 9. Effect of covarying  $T_{\text{IO}}$  on (a) the position of the Hopf bifurcation  $\mu_{\text{crit}}$  and (b) the period of the ENSO mode at  $\mu = \mu_{\text{crit}}$ . Magenta circles: ED case ( $T_{\text{IO}}$  peaks shortly after the maximum of the El Niño index  $N$ ); blue diamonds: LG case ( $T_{\text{IO}}$  peaks after minimum of  $dN/dt$ ); cyan squares: LD case ( $T_{\text{IO}}$  peaks after minimum of  $N$ ); green triangles: EG case ( $T_{\text{IO}}$  peaks after maximum of  $dN/dt$ ). The unfilled magenta circles (cyan squares) correspond to the control of the ED (LD) cases, as explained in the text. Panels (c) and (d) show the growth rate and period for  $a_0 = 0.43 \text{ yr}^{-1}$  and  $\mu = 1$  vs the lag  $\psi$  between  $A$  and  $N$ . A lag value of  $1/4$  means that  $A$  peaks  $1/4$  period later than  $N$ . Positive (negative) values of  $\sigma_r$  indicate growth (damping). Colored markers denote the results for the ED (magenta circle), LG (dark blue diamond), LD (cyan square), and EG (green triangle) cases.

The period in the control cases hardly differs from the 4 yr obtained in the reference case, while  $\mu_{\text{crit}}$  changes from  $\mu_{\text{crit}} = 1$  in the reference case to 1.04 (ED control) and 1.11 (LD control). However, the difference in  $\mu_{\text{crit}}$  between the full ED (LD) case and the corresponding control case is still positive (negative), so apparently the covarying, zero-mean contribution of  $A$  indeed increases (reduces)  $\mu_{\text{crit}}$  [i.e., dampens (destabilizes) the ENSO mode].

To estimate the optimal lag  $\psi$  between  $N$  and  $A$  for which ENSO is most strongly destabilized/stabilized, a set of cases is considered with

$$\frac{dA}{dt} = \cos(\theta)a_0(N - \bar{N}_{\text{ref}}) + \sin(\theta)\frac{a_0}{\omega}\frac{dN}{dt} + a_d A, \quad (14)$$

for  $\theta \in [0, 2\pi]$ . Figures 9c and 9d show the growth rate  $\sigma_r$  and the period  $P$ , respectively, at  $a_0 = 0.43 \text{ yr}^{-1}$  and

$\mu = 1$ , against  $\psi$ . If  $P$  were not affected, then  $\psi = \theta + 0.38 \text{ rad} = \theta + 0.06P$ , but in reality there are slight deviations in that relation. (Note that  $P$  depends on  $\theta$ .) The ENSO mode is most strongly damped if  $\psi = 0.95P$  (i.e., the IO SST peaks  $0.05P$  before  $N$ ); this situation is between the EG and ED case. The strongest destabilization occurs if  $A$  peaks  $0.41P$  later than  $N$ , which is close to the LG case. The period of the ENSO mode at  $\mu = 1$  is shortest if  $A$  lags  $N$  by  $0.19P$  and longest for a lag of  $0.56P$ . These results suggest that the IO damps ENSO and shortens its period, since in observations the lag between the basinwide warming mode and Niño-3.4 is about 3 months and  $P \approx 4 \text{ yr}$  (i.e., the lag is roughly  $0.1P$ ).

Again, the above results can be understood in terms of the easterlies induced by a warm IO. If the  $A$  and  $N$  peaks nearly coincide, then easterlies (westerlies) are induced during El Niño (La Niña), opposing the westerlies (easterlies) induced by the Pacific SST anomalies.

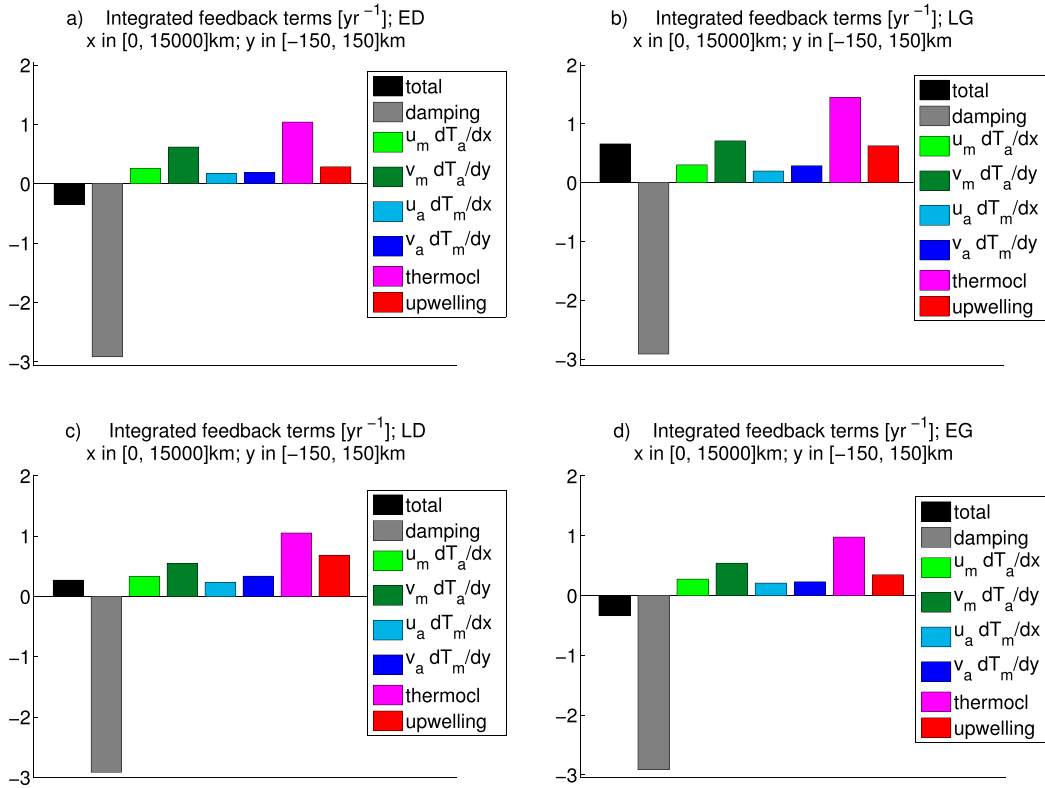


FIG. 10. Bjerknnes feedback contributions for (a) the ED case, (b) the LG case, (c) the LD case, and (d) the EG case, all at  $\mu = 1$ . In all plots, the bars indicate (from left to right) the total growth factor (black), damping (gray), zonal and meridional advection of SST anomalies by equilibrium currents (light and dark green), zonal and meridional advection of equilibrium SST by anomalous currents (light and dark blue),  $T_P - T_{\text{sub}}$  anomalies (thermocline feedback; magenta), and upwelling anomalies (red).

To overcome this damping effect, higher coupling strength in the Pacific is needed; hence  $\mu_{\text{crit}}$  is increased in the EG and ED cases. Similarly, if  $A$  and  $N$  are in antiphase, the IO-induced winds reenforce those of the Pacific, the ENSO mode is destabilized, and  $\mu_{\text{crit}}$  decreases. Concerning the periods, if the lag between  $N$  and  $A$  is about  $1/4$  period, the IO generates easterlies (westerlies) when the winds induced by PO SST switch from westerly to easterly (from easterly to westerly); that is, the switch in wind direction is facilitated and can occur earlier, and hence the period decreases. If, however, the lag is about  $3/4$  periods, the change in wind direction is delayed and the period is lengthened.

Next, we turn to the influence of  $T_I$  on the spatial pattern of the ENSO mode. To exclude the strong influence of  $\mu$  on  $\tilde{\gamma}_{\text{EM}}$ , we evaluate  $\tilde{\gamma}_{\text{EM}}$  at  $\mu = 1$  and  $a_0 = 0.43 \text{ yr}^{-1}$ . For the reference case with  $a_0 = 0$ , we found  $\tilde{\gamma}_{\text{EM}} = 0.36$ . Adding a covarying IO affects  $\tilde{\gamma}_{\text{EM}}$  only slightly. The values are 0.34 (ED), 0.43 (LG), 0.39 (LD), and 0.31 (EG). By construction, as long as  $\mu = 1$ , the background state is independent of  $a_0$ . These changes in  $\tilde{\gamma}_{\text{EM}}$  can be explained as follows. The winds

induced by the IO extend to the PO east coast (Fig. 3b). If  $A$  peaks during El Niño, the IO generates easterlies and hence upwelling near the coast, where the PO-induced wind signal is quite weak. So the IO-induced winds lead to a slight cooling/reduced warming near the coast during El Niño. Hence the coastal SST signal is weakened and  $\tilde{\gamma}_{\text{EM}}$  is reduced in the EG and ED cases, whereas for the LG and LD cases,  $\tilde{\gamma}_{\text{EM}}$  increases. The  $\tilde{\gamma}_{\text{EM}}$  also depends strongly on the background state and  $\mu$ . This explains why the changes in  $\tilde{\gamma}_{\text{EM}}$  for the covarying  $T_I$  cases, for which the background state is fixed, are much smaller than for the constant  $T_I$  cases.

These arguments are confirmed by a Bjerknnes analysis (Fig. 10). The differences in stability between the four cases are mainly due to changes in the thermocline and upwelling feedback. The thermocline feedback is strongest in the LG case. The IO-induced easterlies, peaking shortly after  $N$  becomes negative, cause an additional tilt in the thermocline some time later, which roughly coincides with, and reenforces, La Niña. The upwelling term is about twice as strong for LG and LD than for EG and ED because for LG and LD the

IO-induced easterlies lead to additional upwelling nearly instantaneously, causing additional cooling during La Niña.

#### 4. Summary and conclusions

We have investigated the effect of Indian Ocean (IO) SST on ENSO using a double-basin extension of the Zebiak–Cane model. In this model, the IO's zonally independent SST either covaries with ENSO or is constant. Continuation methods were used to determine the changes in growth rate and spatial pattern of the ENSO mode in the Pacific Ocean (PO) under influence of the IO, in particular focusing on the critical conditions where the growth rate is zero (Hopf bifurcation). We find only one near-critical ENSO mode, as opposed to [Bejarano and Jin \(2008\)](#), who found two such modes in the original ZC model [Zebiak and Cane \(1987\)](#).

For the covarying cases ([section 3c](#)), we found that—depending on the lag between ENSO and IO SST—the growth rate and period of the ENSO mode are affected by the IO. The findings can be explained by bearing in mind that a warm IO leads to easterlies above the Pacific. If a warm IO coincides with El Niño (La Niña), the ENSO-related winds are reduced (enhanced), leading to a damping (growth) of the ENSO mode. This shifts the Hopf bifurcation to higher (lower) values of the coupling strength. If a warm IO occurs during the transition from El Niño to La Niña (from La Niña to El Niño), the ENSO-induced switch in wind direction is facilitated (hampered) and the period decreases (increases). In particular, in the most realistic scenario where El Niño is followed by a warm IO after a few months, the IO dampens El Niño (shift of the Hopf bifurcation to higher coupling strengths) and shortens the period. This result agrees with that in [Frauen and Dommenges \(2012\)](#), who find that decoupling the IO by setting it to climatological values leads to a higher Niño-3 standard deviation and longer periods. [Kug and Kang \(2006\)](#), [Kug et al. \(2006\)](#), and [Santoso et al. \(2012\)](#) suggest that IO warming during the mature phase of El Niño causes easterlies over the PO, which help terminate the event (accelerated phase shift). [Annamalai et al. \(2005\)](#) argue that easterlies due to IO warming during the early phase of El Niño hamper its growth. As the above studies rely solely on either GCMs and/or observations, we think that it is useful to confirm their suggested mechanisms using a simple model, as was done here.

We investigated the effect of long-term trends in the IO SST by putting the IO SST to a constant value different from the radiative equilibrium temperature  $T_0$  ([section 3b](#)). It was found that with a warm IO, the

ENSO mode is destabilized and acquires properties usually associated with central Pacific (CP) El Niños. The ratio between the offshore and coastal SST variability decreases. In case of a very warm IO ( $T - T_0 = 1.125$  K on the equator), the coastal signal again increases in strength but is now nearly in antiphase with the offshore signal. This pattern qualitatively agrees with a strong El Niño Modoki index (EMI) variability ([Ashok et al. 2007](#)). For a cool IO, the ENSO mode is stabilized and becomes less CP-like.

The intensification of ENSO in the warm IO case can be explained by the stronger mean easterlies and equatorial upwelling, as well as a more tilted thermocline, which lead to stronger positive thermocline and upwelling feedbacks. At the eastern coast, however, the temperature  $T_{\text{sub}}$  of the cool upwelling water becomes saturated if the thermocline is too high there, leading to a reduced sensitivity to thermocline variability and weaker signals at the coast. The effect is enhanced by wind anomalies to the east of the strongest SST anomalies, which lead to vertical velocity and temperature anomalies out of phase with the main offshore signal. These results for constant IO are particularly interesting because they offer an explanation for the observed increase in CP activity in the last four decades ([Ashok et al. 2007](#)) in terms of the observed rapid warming of the IO. On the other hand, the predicted intensification of ENSO with increased IO SST has not been identified in observations. Indeed, [Lübbecke and McPhaden \(2014\)](#) find that the Bjerknes index, as constructed from observations, is lower for 2000–10 than for 1980–99. However, 11 years is a very short period to construct the Bjerknes index from data, as regressions have to be made between different variables, and their study does not include the very strong El Niño of 2015/16. Still, it cannot be excluded that our model overestimates the instability (and variability) of CP ENSOs. For example, [Philip and Van Oldenborgh \(2006\)](#) suggest that SST damping might increase in a warming climate owing to enhanced cloud feedbacks, which are not included in our model.

Our mechanism differs from the suggestions in [Yeh et al. \(2009\)](#), who link the increase in CP activity found in CMIP3 projections to decreasing trade winds and a shoaling thermocline in the central PO. Note, however, that [McPhaden et al. \(2011\)](#) found a steepening thermocline and increasing trades in observations for 1980–2010, which is in agreement with our warm IO case. The GCM experiments by [Luo et al. \(2012\)](#) also suggest that easterlies induced by IO warming might lead to a more La Niña-like background state. However, they explain the shift to stronger CP activity by hypothesizing that a steeper thermocline suppresses warm Kelvin waves.

Unfortunately our prediction of a cooling cold tongue is difficult to compare with observations because datasets strongly disagree on SST trends in the tropical Pacific (Deser et al. 2010). However, Fig. 2 of Deser et al. (2010) seems to suggest that the east-central Pacific has at least warmed less than other parts of the tropical ocean.

Note that increasing easterlies over the PO can also be caused by a strengthening of the Hadley circulation or warming in the PO warm pool (PWP). To estimate the latter effect we performed simulations where the PO was warmed over  $0 < x_p < L_p/3$ . The effect on ENSO stability and spatial pattern is very similar to the constant IO case (not shown). In HadISST data for 1970–2011, the equatorial IO (10°S–10°N, 40°–100°E) and the PWP (10°S–10°N, 130°–180°E) warm at a similar rate of  $0.013 \text{ K yr}^{-1}$  (see also Weller et al. 2016); hence the PWP might have a significant effect as well. PWP and IO warming might not be independent. The PWP warming may be partly a response to IO-induced easterlies, and these easterlies may in turn push relatively warm PWP water into the IO via the Indonesian Throughflow (Lee et al. 2015). It might be interesting to investigate whether a significant positive feedback exists between these processes.

The result that ENSO variability depends on the background state may also apply to GCMs (e.g., Guilyardi 2006) and support the suggestion that a correct background state—also of the IO—may be crucial for correct predictions of variability.

Of course, our model is highly idealized in representing the complex interactions within the tropical equatorial climate system. First, the atmospheric response to PO and IO SST is linear (i.e., does not include a detailed representation of convection). Second, the shape of the subsurface temperature  $T_{\text{sub}}$  parameterization, though it has been shown to work well in Zebiak–Cane-type models, does not closely agree with observations. Therefore, it is not clear a priori how strong the effect of the  $T_{\text{sub}}$  saturation for extreme thermocline levels (see section 3b) will be in reality. A comparison of our findings to results from more complex ocean models would be useful here.

Despite these caveats our results suggest that the IO can affect ENSO amplitude and flavor, both through interannual variability and through long-term trends. Warming the PWP may have similar effects as warming the IO. These results offer a possible explanation for the recent increase in CP El Niño activity and suggest that long-term IO (and PWP) trends may play a role for the future of ENSO variability.

*Acknowledgments.* The first author (CW) is sponsored by the NSO User Support Program under Grant

ALW-GO-AO/12-08, with financial support from the Netherlands Organization for Scientific Research (NWO). The authors thank three anonymous reviewers for their helpful comments.

## APPENDIX A

### Model Equations

In this appendix, first the full nondimensional model equations are stated, with emphasis on the effects of adding the Indian Ocean SST. Then some remarks on the discretization scheme are made.

#### a. Nondimensional model equations

The Pacific Ocean basin quantities are nondimensionalized using  $(x_p^*, y_p^*) = (L_p x_p, R_p y_p)$  for the horizontal coordinates,  $t^* = (L_p/c_o)t$  for time,  $\mathbf{u}^* = c_o[u, (R_p/L_p)v, (H_1/L_p)w]$  for the velocity, and  $h^* = Hh$  for the thermocline depth, where the superscript \* denotes dimensional quantities. In the Indian Ocean, coordinates are nondimensionalized as  $(x_I^*, y_I^*) = (L_I x_I, R_I y_I)$ , where  $R_I = R_p$ . The atmospheric equations are nondimensionalized using  $(x_a^*, y_a^*) = (L_a x_a, R_a y_a)$  for the coordinates,  $\mathbf{u}_a^* = c_a[u_a, (R_a/L_a)v_a]$  for the velocity, and  $\phi^* = c_a^2 \phi$  for the geopotential (see Table 1 for dimensional parameters). So each basin and the atmosphere have their own  $x$  coordinates running from 0 to 1. One can transform between the coordinates using (see Fig. 1)

$$\begin{aligned} x_a &= \text{coastw}(b) + [\text{coaste}(b) - \text{coastw}(b)]x_b \\ x_b &= [x_a - \text{coastw}(b)]/[\text{coaste}(b) - \text{coastw}(b)] \\ y_a &= y_b R_b/R_a = \alpha_b y_b, \end{aligned} \quad (\text{A1})$$

where  $\text{coastw}(b)$ ,  $\text{coaste}(b)$  are the positions of the west and east coast of basin  $b$  in atmospheric coordinates. The meridional coordinate  $y$  is zero on the equator.

The equations for the reduced-gravity Pacific Ocean dynamics are as follows:

$$\begin{aligned} (\delta \partial_t + \epsilon_o)u_r - y_p v_r + \partial_{x_p} h &= F_0 \tau_{\text{ext}}^x + \tilde{\mu} u_a \\ y_p u_r + \partial_{y_p} h &= 0 \\ (\delta \partial_t + \epsilon_o)h + \partial_{x_p} u_r + \partial_{y_p} v_r &= 0 \\ \int_{-\infty}^{\infty} u_r(0, y_p, t) dy_p &= 0; u_r(1, y_p, t) = 0 \end{aligned} \quad (\text{A2})$$

and for the embedded surface Ekman layer

$$\begin{aligned}\epsilon_s u_s - y_p v_s &= \gamma_s (F_0 \tau_{\text{ext}}^x + \tilde{\mu} u_a) \\ \epsilon_s v_s + y_p u_s &= \gamma_s \Lambda_0 (F_0 \tau_{\text{ext}}^y + \tilde{\mu} v_a).\end{aligned}\quad (\text{A3})$$

The SST equation in the Pacific Ocean becomes

$$\begin{aligned}\delta \partial_t T_P + u_1 \partial_{x_p} T_P + v_1 \partial_{y_p} T_P + \alpha_w w_1 \mathcal{H}(w_{1P}) \\ \times [T_P - T_{\text{sub}}(h_p)] + \epsilon_T (T_P - T_0) = 0,\end{aligned}\quad (\text{A4})$$

where  $\mathbf{u}_1 = \mathbf{u}_r + \delta_s \mathbf{u}_s$ ,  $\mathcal{H}$  is a mollified Heaviside function,  $\mathcal{H}(w_{1P}) = (1/2)[1 + \tanh(w_{1P}/\delta_w)]$ , and  $T_{\text{sub}}(h) = T_{\text{so}} + (T_0 - T_{\text{so}}) \tanh(\eta_1 h + \eta_2)$ .

Finally, the atmosphere obeys

$$\begin{aligned}\epsilon_a u_a - y_a v_a + \partial_{x_a} \phi &= 0 \\ y_a u_a + \partial_{y_a} \phi &= 0 \\ \epsilon_a \phi + \partial_{x_a} u_a + \partial_{y_a} v_a &= -Q(x_a, y_a, t),\end{aligned}\quad (\text{A5})$$

where  $Q$  is the heating due to deviations of the SST (both Indian or Pacific) from radiative equilibrium (i.e.,  $Q = T - T_0$ ; the proportionality constant is absorbed in  $\mu$ ). The term  $Q$  is expressed in atmospheric coordinates. Since one atmosphere extends over both basins, it can transfer SST signals from the Indian to the Pacific Ocean.

The Indian Ocean temperature is given by

$$\begin{aligned}T_I(x_I, y_I, t) - T_0 &\equiv Q_I(x_I, y_I, t) = T_I^0(x_I, y_I) \times A(t) \\ \frac{dA}{dt} &= a_N N + a_{Nt} \frac{dN}{dt} + a_c + a_d A,\end{aligned}$$

where  $N$  is an El Niño index defined in (A9), and  $T_I^0(x_I, y_I)$  is a prescribed spatial pattern of IO SST anomalies. For a list of nondimensional parameters, see Table A1.

### b. Numerical implementation

As in Van der Vaart et al. (2000), the Pacific quantities are discretized by expanding  $Q_P = T_P - T_0$  (expressed here in Pacific coordinates) into

$$\begin{aligned}Q_P(x_p, y_p) &= \sum_{i=0}^{n_x} \sum_{j=0}^{n_y} \tilde{C}_i(x_p) \psi_j(y_p) q_{ij} \\ &\equiv \sum_{i=0}^{n_x} \sum_{j=0}^{n_y} f_{ij}(x_p, y_p) q_{ij},\end{aligned}\quad (\text{A6})$$

where  $\psi_j$  is the  $j$ th Hermite function and  $\tilde{C}_i(x) \equiv C_i(2x - 1) = \cos[i \arccos(2x - 1)]$  with  $C_i$  being the  $i$ th Chebyshev polynomial. Only the first  $n_x + 1 = 16$  zonal and  $n_y + 1 = 32$  meridional modes are taken into account. Van der Vaart et al. (2000) find only small

TABLE A1. Nondimensional parameters of the Zebiak–Cane model. The coupling strength  $\mu_0$  is set to the location of the Hopf bifurcation in the reference run; the actual coupling strength is given by  $\tilde{\mu} = \mu_0 \mu$ .

Parameter	Meaning	Value
$\epsilon_o = \epsilon_o^* L/c_o$	Ocean damping	0.1
$\epsilon_s = \epsilon_s^* L/c_o$	Surface layer damping	37.5
$\epsilon_a = \epsilon_a^* L_a/c_a$	Atm damping	1.875
$\epsilon_T = \epsilon_T^* L/c_o$	SST damping	0.69
$\alpha_w = H_1/\bar{H}$	Upwelling scale	1.0
$\eta_1 = H/H_*$	$T_{\text{sub}}$ sharpness	5.0
$\eta_2 = h_0/H_*$	$T_{\text{sub}}$ offset	0.75
$\delta_w$	Heaviside sharpness	$5.0 \times 10^{-2}$
$\delta_s$	Ekman contribution scale	0.25
$\delta$	$\partial_t$ term scale	1
$F_0$	$\tau_{\text{ext}}$ scale	0.2
$\alpha = R_p/R_a$	Rosby radii ratio	0.2
$\Lambda_p = R_p/L_p$	PO aspect ratio	$2 \times 10^{-2}$
$\Lambda_a = R_a/L_a$	Atm aspect ratio	$6.7 \times 10^{-2}$
$\gamma_s = (H - H_1)/H_1$	$\mathbf{u}_s$ scale	3
$\mu_0 = \alpha_T \gamma_r L_a L_p \Delta T / (c_a^2 c_o^2)$	Reference coupling strength	4.16

differences between  $n_x = 11, n_y = 21$  and  $n_x = 17, n_y = 41$ . Throughout the present study,  $n_x = 15, n_y = 31$  is used. Henceforth, the shorthand  $\sum_{ij} \equiv \sum_{i=0}^{n_x} \sum_{j=0}^{n_y}$  will be used. The quantity  $r \equiv (u_r + h)/2$  is also decomposed as  $r(x, y) = \sum_{ij} f_{ij}(x, y) r_{ij}$ . The Pacific SST and shallow-water coefficients  $q_{ij}$  and  $r_{ij}$ , together with the IO SST variable  $A(t)$ , form the  $2(n_x + 1)(n_y + 1) + 1 = 1025$ -dimensional state vector  $\mathbf{z}$ , which is sufficient to describe the whole system.

The model is solved using collocation techniques, so the PO quantities are expressed at the zonal points given by

$$x_{P,k} = \frac{1}{2} \left[ 1 + \cos\left(\frac{\pi k}{n_x}\right) \right]; \quad k = 0, 1, \dots, n_x$$

and the meridional points  $y_{P,k}$ , which are the roots of the  $n_y + 1$ th Hermite function. IO quantities are expressed at the same meridional coordinates, whereas in the zonal direction equidistant points are used. Atmospheric quantities are computed at the same locations as ocean quantities, though the positions are expressed using atmospheric coordinates. To solve the atmospheric Eq. (A5), express  $Q_I$  and  $Q_P$  in atmospheric coordinates, write  $Q = Q_P + Q_I$ , rewrite  $u_a = R + S$  and  $\phi = R - S$ , and expand  $R, S, v_a$  and  $Q(x_a, y_a)$  in Hermite functions with the atmospheric meridional coordinate  $y_a$ :  $X(x_a, y_a) = \sum_{j=0}^{n_a} X_n(x_a) \psi_n(y_a)$  for  $X = R, S, v_a, Q$ . Using the recurrence relations for Hermite functions, the system can be rewritten as follows:



$$\begin{aligned}
 (\epsilon_a + \partial_x)R_0(x_a) + \frac{1}{2}Q_0(x_a) &= 0 \\
 R_1(x_a) &= 0 \\
 [(2n - 1)\epsilon_a - \partial_x]R_n(x_a) \\
 + \frac{n - 1}{2} \left[ Q_n(x_a) + \sqrt{\frac{n}{n - 1}}Q_{n-2} \right] &= 0; \quad n \geq 2, \quad (A7)
 \end{aligned}$$

wherein  $Q_n(x_a) = \int Q(x_a, y_a)\psi_n(y_a) dy_a$ .

The equations for  $R$  can be solved and  $S$  and  $v_a$  expressed in terms of  $R$  and  $Q$ . The effect of a unit SST anomaly in the PO basin in mode  $i, j$  can be described by

$$\begin{aligned}
 R_0^{Pij}(x_a) &= -\frac{1}{2}e^{-\epsilon_a x_a} c_{Pj}^0 \int_{\text{coastw}_p}^{\min(x_a, \text{coaste}_p)} e^{\epsilon_a x'_a} \tilde{C}_i[x_p(x'_a)] x_p(x'_a) dx'_a \\
 R_1^{Pij}(x_a) &= 0 \\
 R_n^{Pij}(x_a) &= -\frac{n - 1}{2} e^{\epsilon_a(2n-1)x_a} [c_{Pj}^n + \sqrt{n/(n - 1)}c_{Pj}^{n-2}] \int_{\max(x_a, \text{coastw}_p)}^{\text{coaste}_p} e^{-\epsilon_a(2n-1)x'_a} \tilde{C}_i[x_p(x'_a)] dx'_a, \quad n \geq 2,
 \end{aligned}$$

where  $x_p(x_a)$  is given by (A1) and  $c_{Pj}^n$  is the projection of the  $j$ th Hermite function in the Pacific basin onto the  $n$ th atmospheric Hermite function:  $c_{Pj}^n = \int_{-\infty}^{\infty} \psi_j[y_p(y_a)]\psi_n(y_a) dy_a$ .

The effect of the IO-induced heating is given by

$$\begin{aligned}
 R_0^I(x_a) &= -\frac{1}{2}e^{-\epsilon_a x_a} \int_0^{\min(x_a, \text{coaste}_i)} e^{\epsilon_a x'_a} Q_i^0(x'_a) dx'_a \\
 R_1^I(x_a) &= 0 \\
 R_n^I(x_a) &= -\frac{n - 1}{2} e^{\epsilon_a(2n-1)x_a} \int_{\max(x_a, \text{coastw}_i)}^{\text{coaste}_i} e^{-\epsilon_a(2n-1)x'_a} \left[ Q_i^n(x'_a) + \sqrt{\frac{n}{n - 1}}Q_i^{n-2}(x'_a) \right] dx'_a, \quad n \geq 2.
 \end{aligned}$$

The total  $R_n$  is thus given by  $R_n(x_a) = \sum_{ij} R_n^{Pij}(x_a) + R_n^I(x_a)$ . With this, the zonal wind  $u_a$  over the PO, expressed in the basin coordinates of the PO, is given by

$$u_a(x_p, y_p) = \sum_{ij} \mathcal{A}^{ij}(x_p, y_p) q_{ij} + u_a^I,$$

where  $\mathcal{A}^{ij}$  is the contribution of a unit SST anomaly in mode  $i, j$  in the PO,

$$\begin{aligned}
 \mathcal{A}^{ij}(x_p, y_p) \\
 = \sum_{n=0}^{n_{y,a}} \left\{ R_n^{Pij}[x_a(x_p)] - \sqrt{\frac{n+2}{n+1}} R_{n+2}^{Pij}[x_a(x_p)] \right\} \psi_n(\alpha_p y_p), \quad \text{wherein}
 \end{aligned}$$

and the contribution from the IO is given by

$$\begin{aligned}
 u_a^I(x_p, y_p) \\
 = \sum_{n=1}^{n_{y,a}} \left\{ R_n^I[x_a(x_p)] - \sqrt{\frac{n+2}{n+1}} R_{n+2}^I[x_a(x_p)] \right\} \psi_n(\alpha_p y_p).
 \end{aligned}$$

Similarly,

$$v_a(x_p, y_p) = \sum_{ij} \mathcal{B}^{ij}(x_p, y_p) q_{ij} + v_a^I,$$

$$\begin{aligned}
 \mathcal{B}^{ij}(x_p, y_p) &= \frac{2}{\sqrt{2}} \tilde{C}_i[x_p(x_a)] c_{Pj}^1 \psi_0(\alpha_p y_p) \\
 &+ 2 \sum_{n=1}^{n_{y,a}} \left\{ \sqrt{2(n+1)} \left\{ \epsilon_a R_{n+1}^{Pij}[x_a(x_p)] + \frac{1}{4} \tilde{C}_i[x_p(x_a)] \left( c_{Pj}^{n+1} + \sqrt{\frac{n}{n+1}} c_{Pj}^{n-1} \right) \right\} \psi_n(\alpha_p y_p) \right\},
 \end{aligned}$$

and

$$v_a^I(x_p, y_p) = 2 \sum_{n=1}^{n_{y,a}} \left\{ \sqrt{2n+2} \epsilon_a R_{n+1}^I[x_a(x_p)] \psi_n(\alpha_p y_p) \right\}.$$

As the IO dynamics are ignored, there is no need to express winds over the IO.

With the atmospheric velocities, the Ekman velocities in the PO become

$$\mathbf{u}_s(x_p, y_p) = \tilde{\mu} \sum_{ij} [\mathbf{u}_s^{Pij}(x_p, y_p) q_{ij}] + \tilde{\mu} \mathbf{u}_s^I(x_p, y_p) + \mathbf{u}_s^{\text{ext}}(x_p, y_p),$$

where  $\mathbf{u}_s^{\text{ext}}(x_p, y_p)$  is the contribution from the prescribed background wind. The term  $\mathbf{u}_s^{Pij}(x_p, y_p)$  is the contribution of a unit SST anomaly in mode  $i, j$  in the PO, and  $\mathbf{u}_s^I(x_p, y_p)$  the IO-induced contribution, obeying

$$u_s^{Pij}(x_p, y_p) = \frac{\gamma_s \Lambda_p}{\epsilon_s^2 \Lambda_p^2 + y_p^2} [\epsilon_s \Lambda_p \mathcal{A}^{ij}(x_p, y_p) + y_p \Lambda_a \mathcal{B}^{ij}(x_p, y_p)]$$

$$v_s^{Pij}(x_p, y_p) = \frac{\gamma_s}{\epsilon_s^2 \Lambda_p^2 + y_p^2} [\epsilon_s \Lambda_p \Lambda_a \mathcal{B}^{ij}(x_p, y_p) - y_b \mathcal{A}^{ij}(x_p, y_p)]$$

$$u_s^I(x_p, y_p) = \frac{\gamma_s \Lambda_p}{\epsilon_s^2 \Lambda_p^2 + y_p^2} [\epsilon_s \Lambda_p u_a^I(x_p, y_p) + y_b \Lambda_a v_a^I(x_p, y_p)]$$

$$v_s^I(x_p, y_p) = \frac{\gamma_s}{\epsilon_s^2 \Lambda_p^2 + y_p^2} [\epsilon_s \Lambda_p \Lambda_a v_a^I(x_p, y_p) - y_b u_a^I(x_p, y_p)].$$

The vertical velocity is given by  $w_s(x_p, y_p) = \partial_{x_p} u_s(x_p, y_p) + \partial_{y_p} v_s(x_p, y_p)$ .

The shallow-water equations in the PO can be solved as follows. Expanding  $r \equiv (u_r + h)/2$  and  $s \equiv (u_r - h)/2$  meridionally into Hermite functions yields

$$(\delta \partial_t + \epsilon_o + \partial_{x_p}) r_0(x_p) - \frac{1}{2} \mathcal{F}_0(x_p) = 0$$

$$r_0(x_p = 0) - \sum_{j=2}^{n_y} \frac{\epsilon_j}{j-1} r_j(x_p = 0) = 0$$

$$r_1(x_p) = 0$$

$$[(2j-1)(\delta \partial_t + \epsilon_o) - \partial_{x_p}] r_j$$

$$- \frac{j-1}{2} \left( \mathcal{F}_j - \sqrt{\frac{j}{j-1}} \mathcal{F}_{j-2} \right) = 0, \quad j \geq 2$$

$$r_j(x_p = 1) - \epsilon_j r_0(x_p = 1) = 0, \quad j \geq 2, \quad (\text{A8})$$

with  $\epsilon_0 = 1$ ,  $\epsilon_1 = 0$ ,  $\epsilon_j = \sqrt{j/(j-1)} \epsilon_{j-2}$ ,  $j \geq 2$ . Inserting  $r_j(x_p) = \sum_{i=0}^{n_x} r_{ij} \bar{C}_i(x_p)$  yields a set of coupled linear inhomogeneous ordinary differential equations in  $r_{ij}$ . The forcing terms are given by

$$\mathcal{F}_n(x_p) = F_0 \tau_{\text{ext}}^x + \tilde{\mu} \int_{-\infty}^{\infty} \left[ \sum_{ij} A^{ij}(x_p, y_p) q_{ij}(t) + u_a^I(x_p, y_p, t) \right] \psi_n(y_p) dy_p.$$

For a given set of  $q_{ij}$ ,  $r_{ij}$ , the shallow-water variables are given by

$$u_r(x_p, y_p, t) = \sum_{ij} u_{ij}(x_p, y_p) r_{ij}(t), \quad h(x_p, y_p, t) = \sum_{ij} h_{ij}(x_p, y_p) r_{ij}(t),$$

$$v_r(x_p, y_p, t) = \sum_{ij} v_{ij}^r(x_p, y_p) r_{ij}(t) + \sum_{ij} v_{ij}^q(x_p, y_p) q_{ij}(t) + v^I(x_p, y_p, t) + v^\tau(x_p, y_p),$$

where  $u_{ij}$ ,  $h_{ij}$ , and  $v_{ij}^r$  are linear combinations of the  $f_{ij}$ , while  $v_{ij}^q$ ,  $v_{ij}^I$ , and  $v_{ij}^\tau$  can be expressed in terms of  $\mathcal{A}$ ,  $u_a^I$ , and  $\tau_{\text{ext}}^x$ , respectively, and the Hermite functions  $\psi_n(y_p)$ .

The El Niño index  $N$  is defined as

$$N(t) = q_{00}(t) + q_{10}(t) - \frac{1}{2} q_{20}(t). \quad (\text{A9})$$

Using an index based on low-order (i.e., large spatial scale) SST modes only, rather than the mean SST over a sharp spatial box, reduces numerical errors in our pseudo-spectral implementation of the ZC model.

## APPENDIX B

### Bjerknes Feedback

To compute Bjerknes feedback terms, the SST equation is linearized around the equilibrium solution (denoted here by a bar; anomalies are denoted by plain letters). As trial solution,  $\delta \psi \exp[(\lambda + i\omega)t]$  is used, where  $\delta$  is a small constant, and  $\lambda, \omega \in \mathbb{R}$  and  $\psi \equiv \psi_r + i\psi_i$  the ENSO eigenvector. This yields

$$(\lambda + i\omega)(T_r + iT_i) = -\epsilon(T_r + iT_i) - \bar{u}_1 \partial_x(T_r + iT_i) - \bar{v}_1 \partial_y(T_r + iT_i) - (u_{1r} + iu_{1i}) \partial_x \bar{T} - (v_{1r} + iv_{1i}) \partial_y \bar{T} - \alpha_w \mathcal{M}(\bar{w}_1) \times [T_r + iT_i - T_{\text{sub}}'(\bar{h})] (h_r + ih_i) (\bar{w}_1) \times (w_{1r} + iw_{1i}) [\bar{T} - T_{\text{sub}}(\bar{h})], \quad (\text{A10})$$

where the first line on the rhs denotes damping, the second line advection, and the third and fourth line come from thermocline and upwelling anomalies, respectively.

Summarizing the rhs as  $C_r + iC_i$ , one can solve for the growth factor  $\lambda$  and the frequency  $\omega$  and obtain

$$\begin{aligned}\lambda &= (C_r T_r + C_i T_i)/(T_r^2 + T_i^2) \\ \omega &= (C_i T_r - C_r T_i)/(T_r^2 + T_i^2).\end{aligned}\quad (\text{A11})$$

This yields the real and imaginary parts of the eigenvalue  $\psi$ —no matter at which location the equation is evaluated. Including only certain processes in (A10) will yield their contribution to  $\lambda$  and  $\omega$  at a specific location. To obtain a more global result, we integrate (A10) over  $x = [0, L_P]$  and  $y = [-R_P/2, +R_P/2]$  prior to solving for (contributions to)  $\lambda$  [i.e.,  $C_r, C_i, T_r, T_i$  in (A11) are replaced by their spatial integrals]. Note that a mere rescaling of the temperature anomaly field  $T$  does not affect the damping term (for which  $C \propto T$ ) and also has little effect on advection because  $u_1, v_1$  are dominated by the Ekman contributions, which scale with  $T$ .

#### REFERENCES

- Annamalai, H., S.-P. Xie, and J. P. J. McCreary, 2005: Impact of Indian Ocean sea surface temperature on developing El Niño. *J. Climate*, **18**, 302–319, doi:10.1175/JCLI-3268.1.
- Ashok, K., S. K. Behera, S. A. Rao, H. Weng, and T. Yamagata, 2007: El Niño Modoki and its possible teleconnection. *J. Geophys. Res.*, **112**, C11007, doi:10.1029/2006JC003798.
- Bejarano, L., and F.-F. Jin, 2008: Coexistence of equatorial coupled modes of ENSO. *J. Climate*, **21**, 3051–3067, doi:10.1175/2007JCLI1679.1.
- Capotondi, A., and D. P. Sardeshmukh, 2015: Optimal precursors of different types of ENSO events. *Geophys. Res. Lett.*, **42**, 9952–9960, doi:10.1002/2015GL066171.
- Cessi, P., and F. Paparella, 2001: Excitation of basin modes by ocean-atmosphere coupling. *Geophys. Res. Lett.*, **28**, 2437–2440, doi:10.1029/2000GL012660.
- Chang, P., Y. Fang, R. Saravanan, L. Ji, and H. Seidel, 2006: The cause of the fragile relationship between the Pacific El Niño and the Atlantic Niño. *Nature*, **443**, 324–328, doi:10.1038/nature05053.
- Deser, C., A. S. Phillips, and M. A. Alexander, 2010: Twentieth century tropical sea surface temperature trends revisited. *Geophys. Res. Lett.*, **37**, L10701, doi:10.1029/2010GL043321.
- Dijkstra, H. A., and J. D. Neelin, 1995: Ocean-atmosphere interaction and the tropical climatology. Part II: Why the Pacific cold tongue is in the east. *J. Climate*, **8**, 1343–1359, doi:10.1175/1520-0442(1995)008<1343:OAIATT>2.0.CO;2.
- Dommenget, D., V. Semenov, and M. Latif, 2006: Impacts of the tropical Indian and Atlantic Oceans on ENSO. *Geophys. Res. Lett.*, **33**, L11701, doi:10.1029/2006GL025871.
- Fedorov, A. V., and S. G. Philander, 2000: Is El Niño changing? *Science*, **288**, 1997–2002, doi:10.1126/science.288.5473.1997.
- Frauen, C., and D. Dommenget, 2012: Influences of the tropical Indian and Atlantic Oceans on the predictability of ENSO. *Geophys. Res. Lett.*, **39**, L02706, doi:10.1029/2011GL050520.
- Gill, A. E., 1980: Some simple solutions for heat-induced tropical circulation. *Quart. J. Roy. Meteor. Soc.*, **106**, 447–462, doi:10.1002/qj.49710644905.
- Guillyardi, E., 2006: El Niño–mean state–seasonal cycle interactions in a multi-model ensemble. *Climate Dyn.*, **26**, 329–348, doi:10.1007/s00382-005-0084-6.
- Ham, Y. G., J. S. Kug, and J. Y. Park, 2013: Two distinct roles of Atlantic SSTs in ENSO variability: North tropical Atlantic SST and Atlantic Niño. *Geophys. Res. Lett.*, **40**, 4012–4017, doi:10.1002/grl.50729.
- Izumo, T., and Coauthors, 2010: Influence of the state of the Indian Ocean dipole on the following year's El Niño. *Nat. Geosci.*, **3**, 168–172, doi:10.1038/ngeo760.
- Jansen, M. F., D. Dommenget, and N. S. Keenlyside, 2009: Tropical atmosphere–ocean interactions in a conceptual framework. *J. Climate*, **22**, 550–567, doi:10.1175/2008JCLI2243.1.
- Kao, H.-Y., and J.-Y. Yu, 2009: Contrasting eastern-Pacific and central-Pacific types of ENSO. *J. Climate*, **22**, 615–632, doi:10.1175/2008JCLI2309.1.
- Keller, H. B., 1977: Numerical solution of bifurcation and nonlinear eigenvalue problems. *Applications of Bifurcation Theory*, P. Rabinowitz, Ed., Academic Press, 359–384.
- Kirtman, B. P., 1997: Oceanic Rossby wave dynamics and the ENSO period in a coupled model. *J. Climate*, **10**, 1690–1704, doi:10.1175/1520-0442(1997)010<1690:ORWDAT>2.0.CO;2.
- Klein, S. A., B. J. Soden, and N. C. Lau, 1999: Remote sea surface temperature variations during ENSO: Evidence for a tropical atmospheric bridge. *J. Climate*, **12**, 917–932, doi:10.1175/1520-0442(1999)012<0917:RSSTVD>2.0.CO;2.
- Kug, J. S., and I.-S. Kang, 2006: Interactive feedback between ENSO and the Indian Ocean. *J. Climate*, **19**, 1784–1801, doi:10.1175/JCLI3660.1.
- , T. Li, S.-I. An, I.-S. Kang, J.-J. Luo, S. Masson, and T. Yamagata, 2006: Role of the ENSO? Indian Ocean coupling on ENSO variability in a coupled GCM. *Geophys. Res. Lett.*, **33**, L09710, doi:10.1029/2005GL024916.
- , F.-F. Jin, and S.-I. An, 2009: Two types of El Niño events: Cold tongue El Niño and warm pool El Niño. *J. Climate*, **22**, 1499–1515, doi:10.1175/2008JCLI2624.1.
- Larkin, N. K., and D. E. Harrison, 2005: On the definition of El Niño and associated seasonal average U.S. weather anomalies. *Geophys. Res. Lett.*, **32**, L13705, doi:10.1029/2005GL022738.
- Lee, S.-K., W. Park, M. O. Baringer, A. L. Gordon, B. Huber, and Y. Liu, 2015: Pacific origin of the abrupt increase in Indian Ocean heat content during the warming hiatus. *Nat. Geosci.*, **8**, 445–449, doi:10.1038/ngeo2438.
- Lübbecke, J. F., and M. J. McPhaden, 2014: Assessing the twenty-first-century shift in ENSO variability in terms of the Bjerknes stability index. *J. Climate*, **27**, 2577–2587, doi:10.1175/JCLI-D-13-00438.1.
- Luo, J. J., W. Sasaki, and Y. Masumoto, 2012: Indian Ocean warming modulates Pacific climate change. *Proc. Natl. Acad. Sci. USA*, **109**, 18 701–18 706, doi:10.1073/pnas.1210239109.
- McPhaden, M. J., T. Lee, and D. McClurg, 2011: El Niño and its relationship to changing background conditions in the tropical Pacific Ocean. *Geophys. Res. Lett.*, **38**, doi:10.1029/2011GL048275.
- Met Office Hadley Centre, 2012: Hadley Centre Sea Ice and Sea Surface Temperature data set (HadISST). Met Office Hadley Centre. [Available online at <http://www.metoffice.gov.uk/hadobs/hadisst/>.]
- Philander, S. G., 1990: *El Niño, La Niña, and the Southern Oscillation*. Academic Press, 289 pp.

- Philip, S., and G. J. van Oldenborgh, 2006: Shifts in ENSO coupling processes under global warming. *Geophys. Res. Lett.*, **33**, L11704, doi:10.1029/2006GL026196.
- Rasmusson, E. M., and T. H. Carpenter, 1982: Variations in tropical sea surface temperature and surface wind fields associated with the Southern Oscillation/El Niño. *Mon. Wea. Rev.*, **110**, 354–384, doi:10.1175/1520-0493(1982)110<0354:VITSSST>2.0.CO;2.
- Rayner, N. A., and Coauthors, 2003: Global analyses of sea surface temperature, sea ice, and night marine air temperature since the late nineteenth century. *J. Geophys. Res.*, **108**, 4407, doi:10.1029/2002JD002670.
- Saji, H. N., B. N. Goswami, P. N. Vinayachandran, and T. Yamagata, 1999: A dipole mode in the tropical Indian Ocean. *Nature*, **401**, 360–363.
- Santoso, A., M. H. England, and W. Cai, 2012: Impact of Indo-Pacific feedback interactions on ENSO dynamics diagnosed using ensemble climate simulations. *J. Climate*, **25**, 7743–7763, doi:10.1175/JCLI-D-11-00287.1.
- Van der Vaart, P. C. F., H. A. Dijkstra, and F.-F. Jin, 2000: The Pacific cold tongue and the ENSO mode: A unified theory within the Zebiak–Cane model. *J. Atmos. Sci.*, **57**, 967–988, doi:10.1175/1520-0469(2000)057<0967:TPCTAT>2.0.CO;2.
- Webster, P. J., A. M. Moore, J. P. Loschnigg, and R. R. Leben, 1999: Coupled ocean–atmosphere dynamics in the Indian Ocean during 1997–98. *Nature*, **401**, 356–360, doi:10.1038/43848.
- Weller, E., S. K. Min, W. Cai, F. W. Zwiers, Y. H. Kim, and D. Lee, 2016: Human-caused Indo-Pacific warm pool expansion. *Sci. Adv.*, **2**, e1501719, doi:10.1126/sciadv.1501719.
- Wieners, C. E., W. P. M. de Ruijter, W. Ridderinkhof, A. S. von der Heydt, and H. A. Dijkstra, 2016: Coherent tropical Indo-Pacific interannual climate variability. *J. Climate*, **29**, 4269–4291, doi:10.1175/JCLI-D-15-0262.1.
- Wright, P. B., 1986: Precursors of the Southern Oscillation. *Int. J. Climatol.*, **6**, 17–30, doi:10.1002/joc.3370060103.
- Yeh, S.-W., J.-S. Kug, B. Dewitte, M.-H. Kwon, B. P. Kirtman, and F.-F. Jin, 2009: El Niño in a changing climate. *Nature*, **461**, 511–514, doi:10.1038/nature08316.
- Zebiak, S. E., and M. A. Cane, 1987: A model El Niño–Southern Oscillation. *Mon. Wea. Rev.*, **115**, 2262–2278, doi:10.1175/1520-0493(1987)115<2262:AMENO>2.0.CO;2.